Science  Tr an Sla Tional  Medicine | reSear ch ar Ticle

## RESPIRATORY DISEASE

# TGF-βR2 signaling coordinates pulmonary vascular repair after viral injury in mice and human tissue

Gan Zhao[1,2,3]†, Lulu Xue[4]†, Aaron I. Weiner[1,2,3], Ningqiang Gong[4],
Stephanie Adams-Tzivelekidis[1,2,3], Joanna Wong[1,2,3], Maria E. Gentile[1,2,3], Ana N. Nottingham[3,5],
Maria C. Basil[2,3,5,6], Susan M. Lin[3,5], Terren K. Niethamer[3,5], Joshua M. Diamond[3,5],
Christian A. Bermudez[3,7], Edward Cantu[3,7], Xuexiang Han[4], Yaqi Cao[8], Mohamad-Gabriel Alameh[5],
Drew Weissman[5], Edward E. Morrisey[3,5,6,9], Michael J. Mitchell[4], Andrew E. Vaughan[1,2,3]*

Disruption of pulmonary vascular homeostasis is a central feature of viral pneumonia, wherein endothelial cell (EC) death and subsequent angiogenic responses are critical determinants of the outcome of severe lung injury. A more granular understanding of the fundamental mechanisms driving reconstitution of lung endothelium is necessary to facilitate therapeutic vascular repair. Here, we demonstrated that TGF-β signaling through TGF-βR2 (transforming growth factor–β receptor 2) is activated in pulmonary ECs upon influenza infection, and mice deficient in endothelial *Tgfbr2* exhibited prolonged injury and diminished vascular repair. Loss of endothelial *Tgfbr2* prevented autocrine *Vegfa* (vascular endothelial growth factor α) expression, reduced endothelial proliferation, and impaired renewal of aerocytes thought to be critical for alveolar gas exchange. Angiogenic responses through TGF-βR2 were attributable to leucine-rich α-2-glycoprotein 1, a proangiogenic factor that counterbalances canonical angiostatic TGF-β signaling. Further, we developed a lipid nanoparticle that targets the pulmonary endothelium, Lung-LNP (LuLNP). Delivery of *Vegfa* mRNA, a critical TGF-βR2 downstream effector, by LuLNPs improved the impaired regeneration phenotype of EC *Tgfbr2* deficiency during influenza injury. These studies defined a role for TGF-βR2 in lung endothelial repair and demonstrated efficacy of an efficient and safe endothelial-targeted LNP capable of delivering therapeutic mRNA cargo for vascular repair in influenza infection.

## INTRODUCTION

Viral pneumonia, including that caused by severe acute respiratory syndrome coronavirus 2 (SARS-CoV-2) (*1*) or influenza A (H1N1) infection (*2*), can lead to acute respiratory distress syndrome (ARDS), which has a high mortality rate and poses a large economic burden to society. A primary function of the lung is to serve as a scaffold in support of the pulmonary vasculature to facilitate gas exchange, a concept reinforced by the fact that endothelial cells (ECs) are the most abundant cell type in the lungs (*3*). Emerging evidence further reinforces that ECs are major players in lung injury and viral pneumonia (*4*–*6*). Work from our laboratory and others has demonstrated that endothelial repair upon injury is required for regenerative physiologic outcomes of pneumonia, which is regulated by myriad signals (*7*, *8*). Therapeutic enhancement of endothelial repair therefore represents a promising approach to enabling effective lung repair and preventing mortality in ARDS, but methods to specifically target the lung vasculature are limited. Furthermore, a detailed understanding of the molecular mechanisms involved in effective endothelial repair is lacking.

Vascular repair involves endothelial proliferation, migration, and junctional reannealing, requiring a complex series of coordinated paracrine and intracellular signals (*9*). We previously demonstrated that a venous-associated transcription factor, chicken ovalbumin upstream promoter transcription factor 2, is necessary for effective lung vascular repair, in part by enabling enhanced vascular endothelial growth factor receptor 2 signaling (*8*). However, clear definition of the external signals required for effective lung vascular repair remains elusive. Among pathways involved in angiogenesis, transforming growth factor–β (TGF-β), through binding its receptor TGF-βR2, is a well-described but complex signaling pathway in ECs, wherein receptor activation can be either angiogenic or angiostatic depending on co-receptor expression and signaling cues from the surrounding environment (*10*). Unlike most other cells, TGF-β can act in ECs by engaging two distinct type I receptors, activin receptor–like kinase 1 (ALK1) (*Acvrl1*) and ALK5 (*Tgfbr1*), with opposing effects (*11*). Although ALK5 is broadly expressed in different cell and tissue types, expression of ALK1 is more restricted to ECs (*12*, *13*). Signaling through ALK1 stimulates angiogenesis, promoting EC proliferation and migration by SMAD1/5/8 activation (*12*), whereas the ALK5-dependent pathway through SMAD2/3 phosphorylation is angiostatic and promotes endothelial to mesenchymal transition (*13*), but both pathways require the common type II receptor TGF-βR2. TGF-βR2–mediated signaling is essential for embryonic vascular development, wherein *Tgfbr2*-deficient embryos die at embryonic day 10.5 (E10.5) (*14*). Selective deletion of *Tgfbr2* in ECs causes embryonic lethality because of brain-specific vascular pathologies, including blood vessel morphogenesis and intracerebral hemorrhage (*15*). However, very little is known about TGF-βR2–mediated signaling in lung vascular repair upon viral injury, and given the opposing effects of TGF-β signaling in ECs, it is difficult to predict how

[1]department of Biomedical Sciences, School of Veterinary Medicine, University of Pennsylvania, Philadelphia, Pa 19104, USa. [2]institute for r egenerative Medicine, University of Pennsylvania, Philadelphia, Pa 19104, USa. [3]Penn-cho P l ung Biology institute, University of Pennsylvania, Philadelphia, Pa 19104, USa. [4]department of Bioengineering, University of Pennsylvania, Philadelphia, Pa 19104, USa. [5]department of Medicine, University of Pennsylvania, Philadelphia, Pa 19104, USa. [6]Penn cardiovascular institute, University of Pennsylvania, Philadelphia, Pa 19104, USa. [7]division of cardiovascular Surgery, department of Surgery, Perelman School of Medicine, University of Pennsylvania, Philadelphia, Pa 19104, USa. [8]department of Biostatistics, epidemiology and informatics, University of Pennsylvania Perelman School of Medicine, Philadelphia, Pa 19104, USa. [9]department of cell and developmental Biology, Perelman School of Medicine, University of Pennsylvania, Philadelphia, Pa 19104, USa.
*corresponding author. email: andrewva@vet.upenn.edu
†These authors contributed equally to this work.

engagement of this pathway might affect lung EC regenerative responses.

Although therapeutic targeting of ECs represents a promising route to treat pulmonary vascular disorders (16–18), cell and tissue specificity as well as efficiency and safety remain challenges. Lipid nanoparticles (LNPs) are increasingly recognized as a promising non-viral nanocarrier for gene editing/therapy in vivo, they are relatively easy to synthesize and manufacture (19), and a number of pharmaceuticals using LNPs for drug or mRNA delivery are US Food and Drug Administration approved, including the COVID-19 mRNA vaccines produced by Pfizer/BioNTech and Moderna (20–22). LNPs have also been successfully used for in vivo generation of chimeric antigen receptor (CAR) T cells to treat cardiac fibrosis (23). LNPs have been generated that can target ECs, but most target endothelium across many tissues, transfect additional non-EC types, or are only moderately efficient (24–29).

In the present study, we predicted engagement of TGF-β signaling in the lung endothelium after SARS-CoV-2 and influenza infection by interrogation of single-cell transcriptomics. Using mouse models, human cells, and organoids, we assessed the functional role of this pathway in pulmonary vascular repair. We then determined whether next-generation LNP-mediated mRNA delivery might serve to rescue regenerative angiogenesis in the lung.

## RESULTS

### TGF-βR2 expression is increased in lung ECs upon influenza and SARS-CoV-2 injury in mice and humans

In influenza-induced viral pneumonia, although the virus rarely infects ECs, vascular injury is caused by secondary effects, especially overexposure to inflammatory cytokines. Thick section imaging demonstrated disruption of the vascular network [vascular endothelial cadherin (VECAD)], reduced lectin perfusion, and disorganization of pericyte coverage (neuron-glial antigen 2) by day 15 after infection with H1N1 influenza (PR8) (fig. S1A). More apoptotic ECs [terminal deoxynucleotidyl transferase–mediated deoxyuridine triphosphate nick end labeling–positive (TUNEL+) erythroblast transformation-specific (ETS)–related gene (ERG+)] were also observed at day 15 after infection compared with mock-infected controls (fig. S1B). These data reinforce previous studies confirming that ECs are lost during influenza injury and subsequently regenerate (7, 8).

We reanalyzed publicly available human snRNA-seq (single-nucleus RNA sequencing) datasets collected (30) from lungs of both healthy patients (n = 7) and patients with COVID-19 (n = 19) (Fig. 1A and fig. S2A). ECs were subsetted and reclustered for further analysis based on endothelial marker expression (Fig. 1, B and C, and fig. S2, B to D). Both TGFBR2 and its downstream SMAD signaling pathway–related genes (SMAD1 and SMAD3) exhibited up-regulation in ECs from patients with lethal COVID-19 (Fig. 1, C and D, and fig. S2F), indicating a potential role for the TGF-βR2–mediated signaling pathway in the endothelial response to viral injury. We observed that TGF-BR2 is broadly expressed in human EC types (fig. S2E). Quantitative immunostaining and reverse transcription quantitative polymerase chain reaction (RT-qPCR) of sorted lung ECs confirmed increased expression of TGFBR2 in ECs in the lungs of patients after COVID-19 infection (see Materials and Methods) (Fig. 1, E and F).

Single-cell RNA-seq (scRNA-seq) analysis for mouse lung ECs sorted from uninjured and postinfluenza lungs (days 0, 20, and 30, respectively) recapitulated these findings, where Tgfbr2 expression was elevated in mouse lung ECs from day 20 and day 30 (Fig. 1, G to J), including specifically within blood vascular ECs. The proliferating EC population exhibited elevated expression of Tgfbr2 (fig. S3, A to H). We also observed increased expression of Tgfbr2 in sorted mouse lung ECs during influenza injury (Fig. 1K). Nearly all SMAD genes were up-regulated in injured mouse ECs (Fig. 1L), suggesting not only increased sensitivity to ligands but also possible activation of TGF-βR2–mediated signaling in influenza-injured lung endothelium.

### Endothelial loss of TGF-βR2 prevents effective recovery from influenza-induced lung injury

To investigate the functional role of TGF-βR2 in pulmonary endothelial repair, we crossed VECAD^CreERT2 mice with Tgfbr2^flox mice (31) to generate homozygous mutant mice and proceeded with Tgfbr2 deletion (Tgfbr2^ECKO) in adult mice through tamoxifen administration. Unchallenged mice did not exhibit any overt phenotypes 2 months after Tgfbr2 deletion (fig. S4, A to D). Upon influenza infection, although all mice showed equivalent disease induction (including weight loss and impaired oxygen saturation) for the first ~9 days, Tgfbr2^ECKO (VECAD^CreERT2; Tgfbr2^flox/flox) mice demonstrated prolonged morbidity, including longer body weight recovery time and decreased capillary oxygen saturation between 16 and 26 days after infection (Fig. 2, A and B). Moreover, survival was reduced in Tgfbr2^ECKO animals (Fig. 2C). In addition, we observed that endothelial deficiency of Tgfbr2 resulted in more severe local inflammation and increased vascular permeability during viral injury, which was demonstrated by total protein concentration (Fig. 2D), myeloperoxidase (MPO) activity (Fig. 2E), and fluorescein isothiocyanate–dextran leak (Fig. 2F) into bronchoalveolar lavage fluid (BALF). However, loss of Tgfbr2 in ECs did not affect viral load (fig. S5A).

To assess whether EC proliferation was affected by Tgfbr2 loss, we performed flow cytometry analysis at day 15 after influenza infection, observing that Tgfbr2-deficient ECs were less proliferative (Fig. 2, G and H, and fig. S5B), indicating that reduced angiogenic proliferative capacity contributed to the increased pathology. qRT-PCR of sorted ECs on day 20 after infection confirmed deletion of Tgfbr2 accompanied by reduced mki67 expression in Tgfbr2^ECKO mice (Fig. 2I). Histologic analysis of the Tgfbr2^ECKO lungs in the mice that survived demonstrated more severe injury, as judged by a previously described unbiased computational imaging approach (Fig. 2, J to L) (32). Furthermore, the evaluation of vascular endothelial repair through staining of the vascular integrity marker, VECAD, in each injury zone [defined in (32)] revealed that endothelial Tgfbr2 deficiency led to reduced vascular density and continuity within the damaged area (Fig. 2, M to O). Representative confocal microscopy further reinforced the severity of injury indicated by the quantitative functional and fluorescence-activated cell sorting analysis, with Tgfbr2^ECKO lungs exhibiting less vessel reorganization/remodeling and lower capillary density through day 27 (fig. S5C). Despite TGF-β's role in promoting fibrosis in numerous contexts, we did not observe any impact of endothelial Tgfbr2 deficiency on the development of pulmonary fibrosis in influenza viral pneumonia (fig. S5D). We also did not observe any morphological differences in ECs (including arterial ECs, venous ECs, lymphatic ECs, and capillary ECs) due to the deletion of Tgfbr2 (fig. S6, A to D).

### Endothelial TGF-βR2 deficiency impedes CAR4+ aerocyte renewal upon influenza-induced lung injury

Among lung ECs, carbonic anhydrase IV (Car4)–expressing aerocytes ("aCaps" and "Cap2s") are thought to be specialized for gas

Zhao et al., Sci. Transl. Med. 16, eadg6229 (2024) 31 January 2024

2 of 15
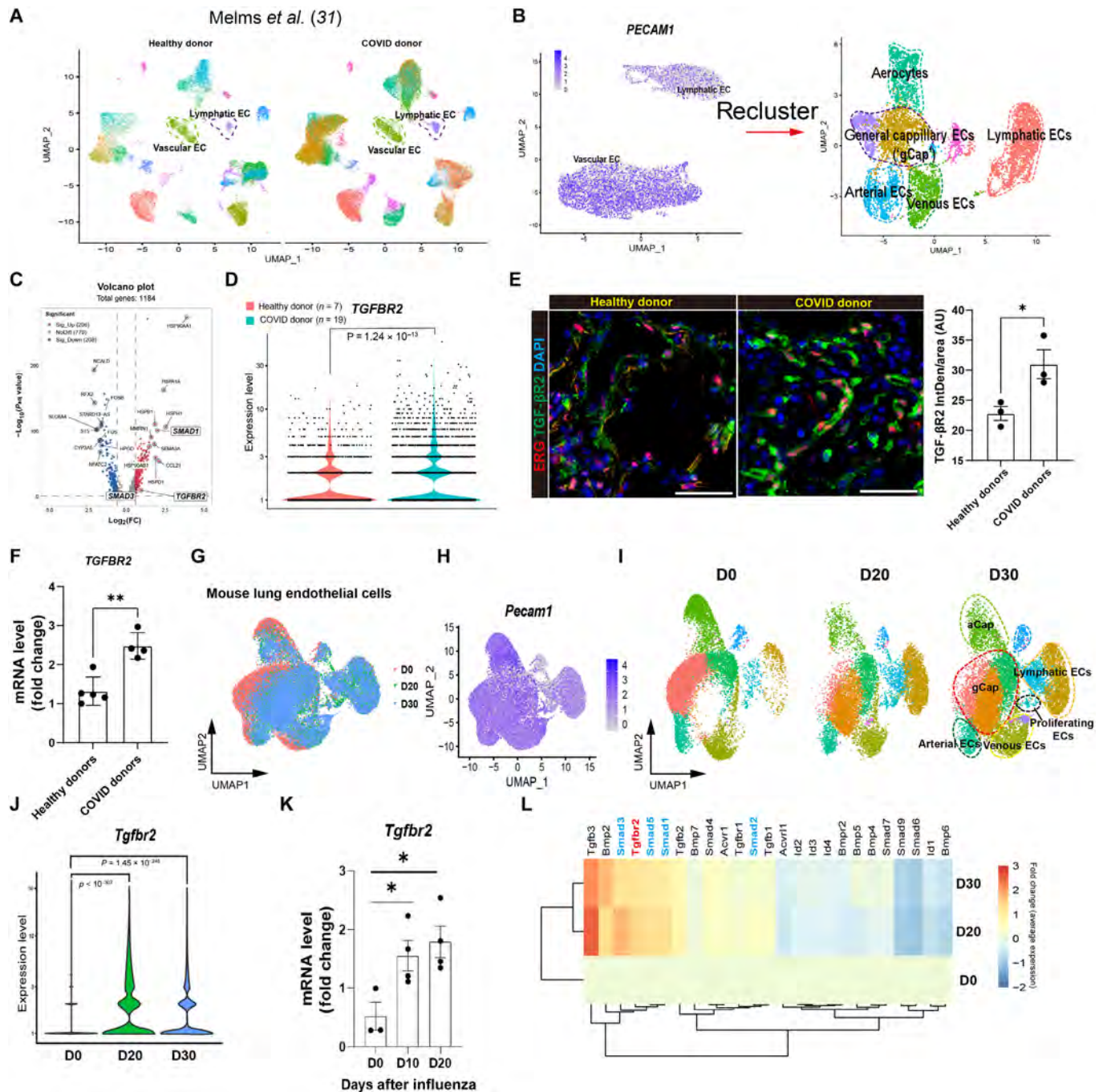
**Fig. 1. Up-regulation of *TGFBR2* and TGF-βR2–mediated signaling after viral injury.** (**A**) reanalysis of published snrna-seq datasets of healthy (*n* = 7 donors) and coVid (*n* = 19 donors) lungs from Melms *et al.* (*30*), with ec clusters labeled. (**B**) left: endothelial clusters were subsetted from (a) and confimed by signature ec gene *PECAM1* (cd 31). right: Uniform Manifold approximation and Projection (UMaP) plot of reclustered ec populations. (**C**) Volcano plot displaying differentially expressed genes in healthy and coVid lung ecs. Fc, fold change. (**D**) Violin plot of *TGFBR2* mrna expression (log-normalized) in ecs. $P = 1.24 \times 10^{-13}$ was determined by Wilcoxon rank-sum test. (**E**) left: representative immunofluoescence image of endothelial (erG+) TGF-βr2–expressing cells in both healthy and post-coVid lung tissue. Scale bar, 50 µm. right: Quantifiction of TGF-βr2 immunostaining (healthy donors, *n* = 3; coVid donors, *n* = 3). inden, integrated density. data are means ± SeM, unpaired two-tailed *t* test, *$P = 0.038$. daPi, 4′,6-diamidino-2-phenylindole; aU, arbitrary units. (**F**) qPcr analysis of *TGFBR2* in sorted human lung ecs from both healthy (*n* = 5) and post-coVid (*n* = 4) donors. data are means ± Sd, unpaired two-tailed *t* test, **$P = 0.002$. (**G**) scrna-seq analysis for mouse lung ecs sorted from uninjured (d0) and on 20 and 30 days after influenza infection (marked as d20 and d30, respectively). (**H**) UMaP plot showing ec marker gene (*Pecam1*). (**I**) UMaP plot of ec populations annotated in scrna-seq data for adult mouse lung (*34, 57*). (**J**) Violin plots showing *Tgfbr2* expression in mouse lung ecs sorted from d0, d20, and d30, respectively. *P* value was determined by Wilcoxon rank-sum test, d0 versus d20, $P < 10^{-307}$; d0 versus d30, $P = 1.45 \times 10^{-248}$. (**K**) qPcr analysis of *Tgfbr2* in isolated lung ecs (cd 45−cd 31+) sorted on day 0 (uninjured) and on days 10 and 20 after influenza infection. *n* = 3 or 4 per group; data are presented as means ± SeM, unpaired two-tailed *t* test. *d0 versus d10, $P = 0.0326$; d0 versus d20, $P = 0.0198$. (**L**) heatmap comparing TGF-β pathway gene expression in mouse lung ecs sorted from d0, d20, and d30, respectively.

Zhao *et al.*, *Sci. Transl. Med.* **16**, eadg6229 (2024)   31 January 2024

**3 of 15**
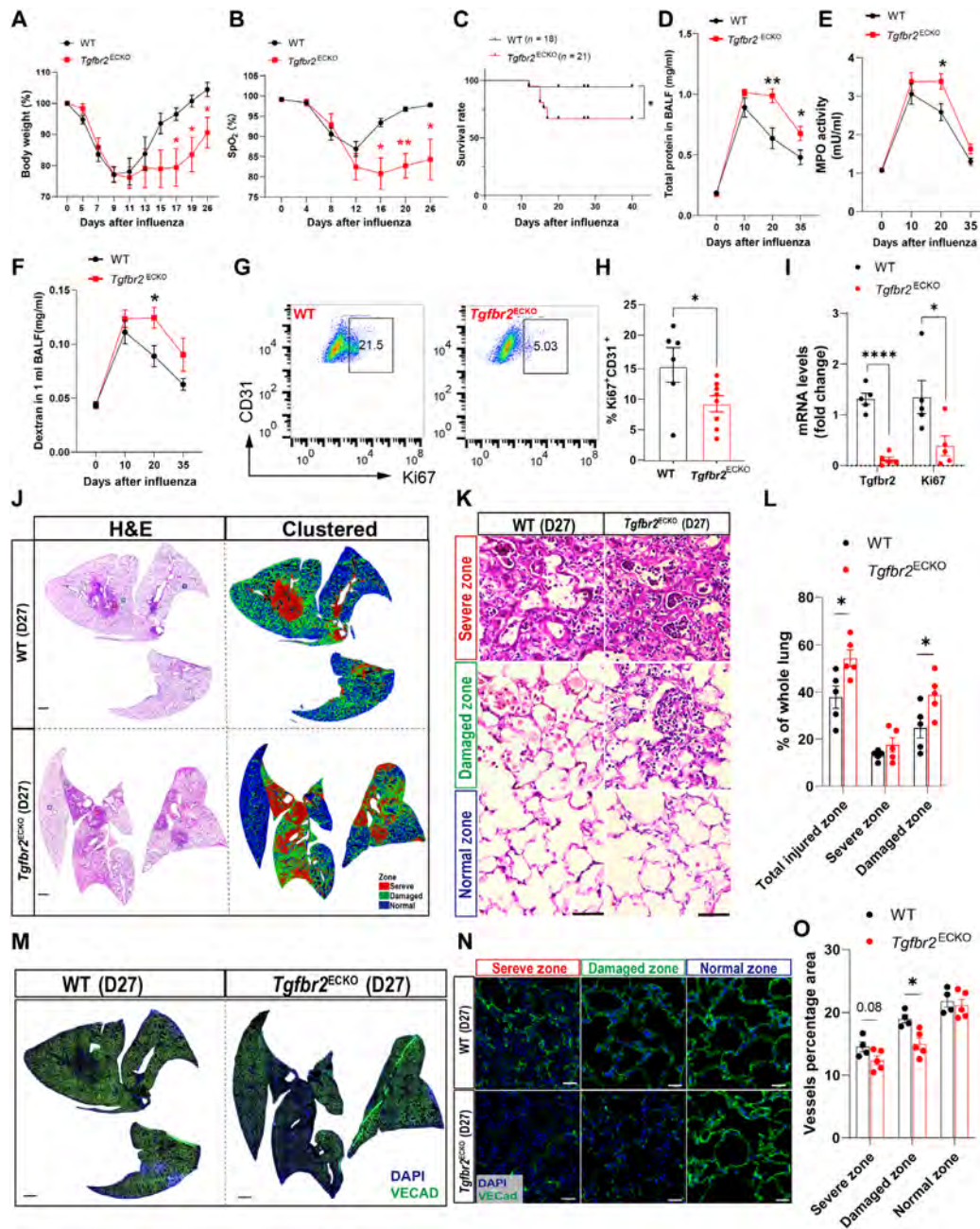
**Fig. 2. Endothelial *Tgfbr2* deletion invivo prevents EC repair after influenza injury.** (**A** and **B**) Vecad^creer T2; *Tgfbr2*^fl x/fl x or WT (Vecad^creer T2 or *Tgfbr2*^fl x/fl x) mice were administered fi e doses of tamoxifen, followed by 3 weeks of chase and influenza infection. Time course of changes in capillary oxygen saturation (a) and body weight (B) in WT and *Tgfbr2*^ecKo mice, *n* = 5 to 8 per group. data are means ± SeM, unpaired two-tailed *t* test; *\*P* < 0.05 and *\*\*P* < 0.01. WT versus *Tgfbr2*^ecKo in (a): d 17, *P* = 0.028; d 19, *P* = 0.018; d26, *P* = 0.034. WT versus *Tgfbr2*^ecKo in (B): d 16, *P* = 0.01; d 20, *P* = 0.0013; d 26, *P* = 0.019. (**C**) Kaplan-Meier survival curves after influenza infection, log-rank test. data are means ± SeM, *\*P* = 0.0477. (**D** to **F**) Total protein (d), MPo activity (e), and perfused dextran (F) were quantified in Bal F on day 0 (uninjured, *n* = 3 mice), day 10 (*n* = 4 mice), day 25 (*n* = 5 mice), and day 35 (*n* = 5 mice) after influenza infection. data are means ± SeM, unpaired two-tailed *t* test, *\*P* < 0.05 and *\*\*P* < 0.01. WT versus *Tgfbr2*^ecKo in (d): d20, *P* = 0.009; d35, *P* = 0.047. WT versus *Tgfbr2*^ecKo in (e): d20, *P* = 0.028. WT versus *Tgfbr2*^ecKo in (F): d20, *P* = 0.032. (**G** and **H**) intracellular fl w cytometry quantific tion of proliferative ec s (cd 45^−/epca M^−/cd 31^+/Ki67^+) at day 15 after influenza. WT, *n* = 6; *Tgfbr2*^ecKo, *n* = 8. data are means ± SeM, unpaired two-tailed *t* test, *\*P* = 0.0412. (**I**) qPcr analysis of *Tgfbr2* and *Mki67* in isolated lung ec s (cd 45^−cd 31^+) from WT and *Tgfbr2*^ecKo mice sorted 20 days after influenza infection. data are means ± SeM (*n* = 5), unpaired two-tailed *t* test, *\*P* < 0.05 and *\*\*\*\*P* < 0.0001. *Tgfbr2*, *P* < 0.0001; *Mki67*, *P* = 0.036. (**J**) l eft: Tile scan images of h &e stain at 27 days after infection; demarcated boxes indicate different injury zones. r ight: c lustered injury zone maps produced from left h &e images. Scale bars, 1 mm. (**K**) Zoomed-in images from the demarcated boxed area in (J). Scale bars, 50 µm. (**L**) Quantifi cation of injured area in different injury zones in (J). data are means ± SeM (*n* = 5), unpaired two-tailed *t* test, *\*P* < 0.05. Total injured zone, *P* = 0.024; damaged zone, *P* = 0.039. (**M**) Tile scan images of immunostaining of vascular endothelial cadherin (Vec ad ) at day 27 after infection. Scale bars, 1 mm. (**N**) images of Vec ad staining in different injury zones in (M). Scale bars, 25 µm. (**O**) Quantific tion of vessel percentage judged by Vec ad staining in different injury zones in (M). data are means ± SeM (*n* = 5), unpaired two-tailed *t* test, *\*P* < 0.05. Total injured zone, *P* = 0.08; severe zone, *P* = 0.011.

exchange and the trafficking of leukocytes, whereas "general" capillary ECs ("gCaps" and "Cap1s") function as stem/progenitor cells (*33*, *34*). We observed that CAR4$^+$ ECs were reduced on day 15 but replenished by day 30 after infection (fig. S7A). We then asked whether blockade of TGF-βR2 signaling might impair aerocyte restoration upon influenza injury. Intracellular flow cytometry for CAR4$^+$ ECs on days 0, 20, and 35 after infection quantitatively confirmed aerocyte loss (Fig. 3, A and B). Reduction in total lung ECs in *Tgfbr2*$^{ECKO}$ mice at day 35 after infection was observed (Fig. 3C), reinforcing the finding of decreased pulmonary vessel density in *Tgfbr2*$^{ECKO}$ mice (Fig. 2, M to O, and fig. S5C). Immunostaining and qPCR of sorted ECs for aerocyte genes (*34*), including *Apln* (Apelin), *Tbx2* (T-box transcription factor 2), and *Car4*, further validated the observed reduction in CAR4$^+$ aerocytes in *Tgfbr2*$^{ECKO}$ mice at day 20 after infection compared with controls (Fig. 3, D and E). Aerocytes have also been characterized by high expression of endothelin receptor B (*Ednrb*) and *CD34* (*7*). Similarly, our data demonstrated impaired recovery of EDNRB$^+$ and CD34$^+$ ECs in *Tgfbr2*$^{ECKO}$ mice at day 35 after infection compared with controls (Fig. 3, F to H, and fig. S7B). We noted that *Vegfa* was decreased in *Tgfbr2*$^{ECKO}$ mouse ECs (Fig. 3E). However, we did not observe any effect on the expression of other typical angiogenic factors in ECs, including *Angpt2*, *Fgf1*, *Pdgfa*, and *Pdgfb* (fig. S7C). We observed that the concentration of vascular endothelial growth factor A (VEGFA) in the BALF increased during viral pneumonia, followed by a subsequent decrease, reaching its peak at day 20, which coincided with the peak stage of angiogenic repair (fig. S7D). Endothelial *Tgfbr2* deficiency reduced total VEGFA protein in BALF (fig. S7D), although it did not have an impact on the expression of *Vegfa* from other cell sources (fig. S7E).

## Leucine-rich α-2-glycoprotein 1 coordinates TGF-βR2 signaling to mediate angiogenic repair

To further characterize the molecular mechanisms underlying TGF-βR2–mediated endothelial regeneration in vivo, we assessed the effects of TGF-βe stimulation in vitro in immortalized human lung microvascular ECs (iMVECs) (*8*, *35*). Upon TGF-β1 treatment, Western blotting detected SMAD2/3 and SMAD1/5 phosphorylation, as predicted by studies in other vascular EC types (*11*, *36*). Deletion of *TGFBR2* completely prevented phosphorylation of both SMAD types (fig. S8, A to C). Cell proliferation assays revealed that TGF-β1 inhibited proliferation of iMVECs, whereas *TGFBR2* deletion completely blocked this effect (fig. S8D), indicating that although both arms of the TGF-βR2 pathway are activated by the TGF-β ligand in ECs, the overriding response is angiostatic.

These results were seemingly incongruent with the observation that *Tgfbr2* deletion inhibits EC proliferation in vivo, so we speculated that other signaling molecules must be involved to promote proangiogenic signaling through TGF-βR2. Leucine-rich α-2-glycoprotein 1 (LRG1), a proangiogenic factor that operates by shunting endothelial TGF-β signaling toward SMAD1/5 activation and proliferation at the expense of angiostatic signaling through SMAD2/3 (*36*), was greatly up-regulated in injured ECs (Fig. 4A and fig. S9A). Sorted primary lung ECs exhibited marked *Lrg1* up-regulation by 10 days after infection, which gradually normalized as endothelial repair was completed (Fig. 4B). In addition, LRG1 protein in BALF and serum increased on day 15 after infection and decreased gradually with recovery (Fig. 4, C and D). The concentration of TGF-β1 remained low until late time points after infection (Fig. 4, C and D), whereas the peak period of LRG1 up-regulation coincided with active EC proliferation. We

observed coincident increase in activated endothelial SMAD1/5 signaling (pSMAD1/5$^+$ERG$^+$) at this time (fig. S9B). Subsequently, this signaling decreased on day 27 after infection, whereas the angiostatic SMAD2/3 signaling (pSMAD3$^+$ERG$^+$) exhibited an opposite trend (fig. S9C). This appeared to be associated with increased LRG1 in the vascular niche. To test this, we used a lung endothelium–targeted LNP (LuLNP) delivery system (described in Fig. 6), which enables the specific and efficient delivery of small interfering RNA (siRNA) (si-Lrg1) to lung ECs, leading to reduction in endothelial *Lrg1* expression (Fig. 4, E and F) and LRG1 protein in both serum and BALF during viral injury (fig. S10, A and B). Experimental reduction of LRG1 by si-*Lrg1* delivery led to a decrease in the activation of SMAD1/5 during injury, whereas we observed little impact on SMAD3 activation (Fig. 4G and fig. S10, C and D). Furthermore, knockdown of *Lrg1* impeded endothelial angiogenic proliferation (Fig. 4H and fig. S10E).

We further probed the consequences of LRG1 and TGF-β1 stimulation in vitro in human primary lung ECs. Recognizing that SMAD1/5 and SMAD2/3 can show differential responsiveness to concentrations of TGF-β ligands (*11*), we tested the effects of LRG1 with two different concentrations of TGF-β1. With TGF-β1$^{lo}$ (3 ng/ml), phosphorylation of SMAD2/3 was increased, but SMAD1/5 phosphorylation was not. Adding recombinant LRG1 enhanced SMAD1/5 phosphorylation, but SMAD2/3 phosphorylation was inhibited compared with TGF-β1 treatment alone. Given TGF-β1$^{hi}$ (10 ng/ml), LRG1 increased the phosphorylation of both SMAD2/3 and SMAD1/5, although the effect was more pronounced for SMAD2/3 (Fig. 4, I-K). We further confirmed by 5-ethynyl-2′-deoxyuridine (EdU) incorporation assay that the TGF-β1$^{lo}$ + LRG1 conditions increased EC proliferation, whereas the high concentration of TGF-β1 with or without LRG1 inhibited EC proliferation (Fig. 4, L and M). Low concentrations of TGF-β1 (TGF-β1$^{lo}$) and high amounts of LRG1 activate proangiogenic, SMAD1/5 phosphorylation, whereas with high concentrations of TGF-β1, LRG1 enhances both SMAD1/5 and SMAD2/3 signaling (fig. S9D).

We again used iMVECs to confirm these observations, generating constitutively overexpressing LRG1 (LRG1-OE) cells (fig. S8, E and F) and treating them with escalating concentrations of TGF-β1 (0 to 20 ng/ml). LRG1 enhanced TGF-β1–induced phosphorylation of both SMAD1/5 and SMAD2/3 when the TGF-β1 concentration was higher than 5 ng/ml in culture medium, whereas LRG1 preferentially promoted SMAD1/5 phosphorylation at lower TGF-β1 concentrations (fig. S8G). Functionally, LRG1-OE iMVECs demonstrated increased proliferative and migratory ability, whereas high concentrations of TGF-β1 (10 ng/ml) reduced the angiogenic effects of LRG1 (fig. S8, H to K). The fact that the concentration of TGF-β1 started to increase ~20 days after infection (Fig. 4, C and D), during which vascular repair enters a stable phase, further indicated that TGF-β1 counteracts the LRG1-mediated angiogenic response. When *TGFBR2* knockout (KO) iMVECs (generated by lentiviral delivery of CRISPR-Cas9; fig. S8, A to C) were treated with recombinant LRG1 protein (5 μg/ml), the angiogenic proliferation otherwise induced by LRG1 was lost (fig. S8D), indicating that LRG1-mediated angiogenic effects remain dependent on TGF-βR2.

## VEGFA rescues insufficient angiogenesis caused by TGF-βR2 deficiency in vitro

VEGFA is the prototypical angiogenic growth factor with critical roles in angiogenesis during development and repair. We observed decreased EC *Vegfa* expression in uninjured mice (Fig. 5A) and VEGFA
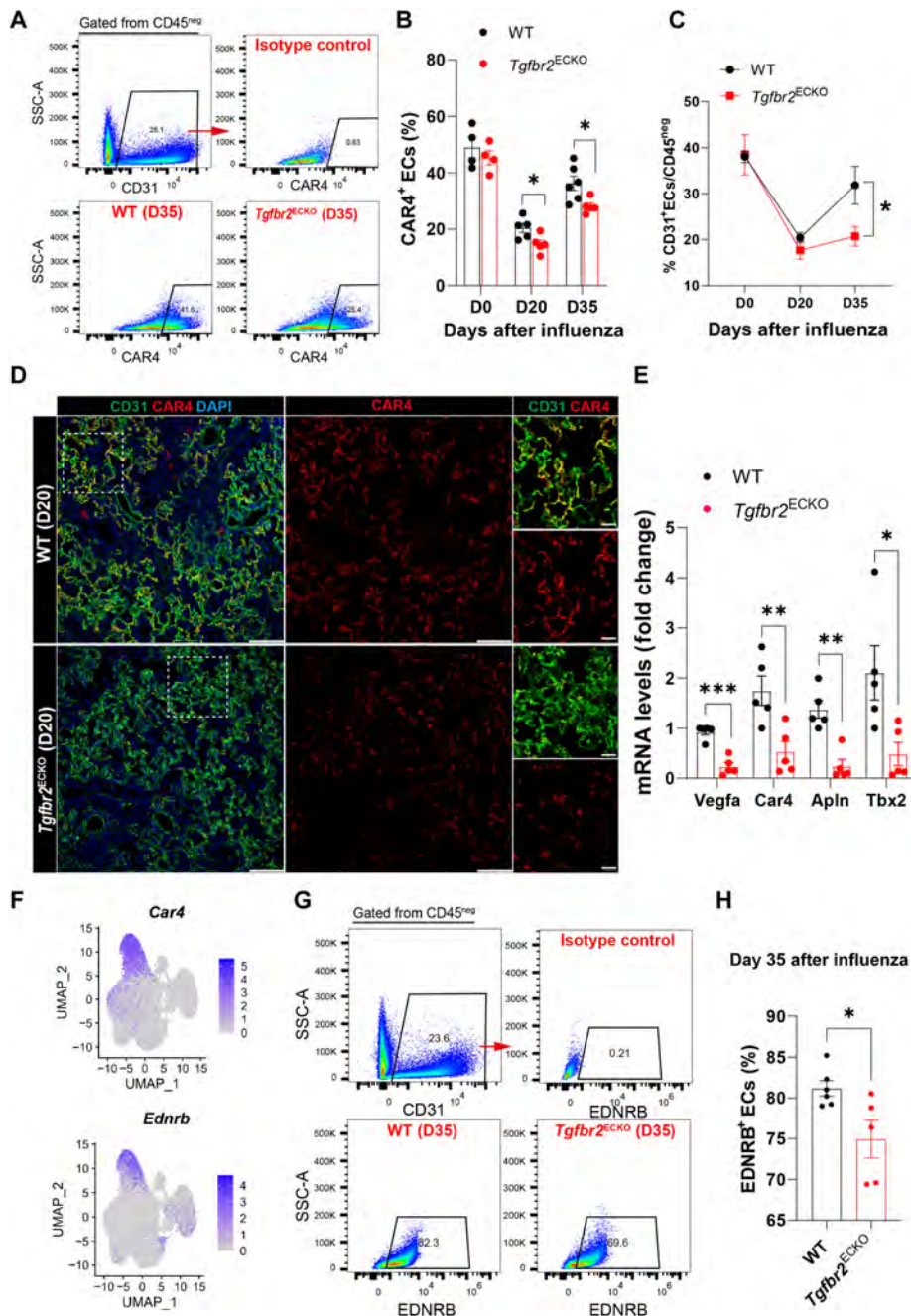
**Fig. 3. Endothelial *Tgfbr2* deletion in vivo impairs aerocyte regeneration after influenza injury.** (**A**) representative gating scheme for identification of car4-expressing aerocyte ecs at day 35 after influenza infection. SSc-a, side scatter area. (**B**) intracellular flow cytometry quantification of car4-expressing aerocyte ecs at day 0 (uninjured; WT, $n = 4$; *Tgfbr2*[ecKo], $n = 4$), day 20 (WT, $n = 5$; *Tgfbr2*[ecKo], $n = 5$), and day 35 (WT, $n = 6$; *Tgfbr2*[ecKo], $n = 5$) after influenza infection. data are means ± SeM, unpaired two-tailed *t* test, *$P < 0.05$. d20, $P = 0.033$; d35, $P = 0.026$. (**C**) The percentage of lung ecs was compared between WT and *Tgfbr2*[ecKo] mice at day 0 (uninjured; WT, $n = 3$; *Tgfbr2*[ecKo], $n = 3$), day 20 (WT, $n = 5$; *Tgfbr2*[ecKo], $n = 5$), and day 35 (WT, $n = 6$; *Tgfbr2*[ecKo], $n = 5$) after influenza infection. data are means ± SeM, unpaired two-tailed *t* test, *$P = 0.037$. (**D**) representative immunostaining of car4-expressing aerocytes in WT and *Tgfbr2*[ecKo] mice on day 20 after infection. Scale bars, 100 and 25 μm (inset). (**E**) qPcr analysis of aerocyte genes *Car4*, *Apln* and *Tbx2* in isolated total lung ecs (cd45⁻cd31⁺) from WT and *Tgfbr2*[ecKo] mice sorted on day 20 after influenza infection. WT, $n = 5$; *Tgfbr2*[ecKo], $n = 5$. data are means ± SeM, unpaired two-tailed *t* test, *$P < 0.05$, **$P < 0.01$, and ***$P < 0.001$. *Vegfa*, $P = 0.00014$; *Car4*, $P = 0.009$; *Apln*, $P = 0.0009$; *Tbx2*, $P = 0.024$. (**F**) Feature plots showing *Car4* and *Ednrb* expression in aerocyte ecs. (**G**) representative gating scheme for identification of ednrB-expressing ecs at day 35 after influenza infection. (**H**) intracellular flow cytometry quantification of ednrB-expressing ecs at day 35 (WT, $n = 6$; *Tgfbr2*[ecKo], $n = 5$) after influenza infection. data are means ± SeM, unpaired two-tailed *t* test, *$P = 0.026$.

protein during influenza infection (fig. S7D) with *Tgfbr2*[ECKO] mice. In addition, TGF-β1 has been shown to promote *Vegfa* expression through SMAD signaling in tumor angiogenesis (*37*). We confirmed that TGF-β1 treatment induced *Vegfa* expression in vitro, which was abolished by *TGFBR2* KO (Fig. 5B).

We hypothesized that exogenous VEGFA supplementation might partially rescue impaired vascular repair caused by endothelial *TGF-BR2* depletion. To test this, we used human induced pluripotent stem cells (hiPSCs) to generate vascular networks/vascular organoids on the basis of published protocols (Fig. 5, C and D) (*38*). Treatment with TGF-βR2 inhibitor (*39*) ITD-1 (10 μM) during differentiation reduced vascular network density and organoid formation efficiency, whereas further addition of recombinant VEGFA protein ameliorated

insufficient angiogenesis caused by TGF-βR2 blockade (Fig. 5, E to G). Because vascular organoids also contain pericytes that might respond to ITD-1 and thus indirectly affect angiogenesis, we performed knockdown of *TGFBR2* in human primary lung ECs using *TGFBR2* siRNA (si-*TGFBR2*) (Fig. 5H and fig. S11, A and B). *TGFBR2* knockdown inhibited tube formation, which was effectively rescued by addition of VEGFA (20 ng/ml) (Fig. 5I).

## An LNP delivery system specifically targets the lung endothelium

A collaborative effort identified a potential lung endothelial–specific LNP formulation, LuLNP (details described in Materials and Methods; fig. S12, A to D). Green fluorescent protein (GFP) mRNA was
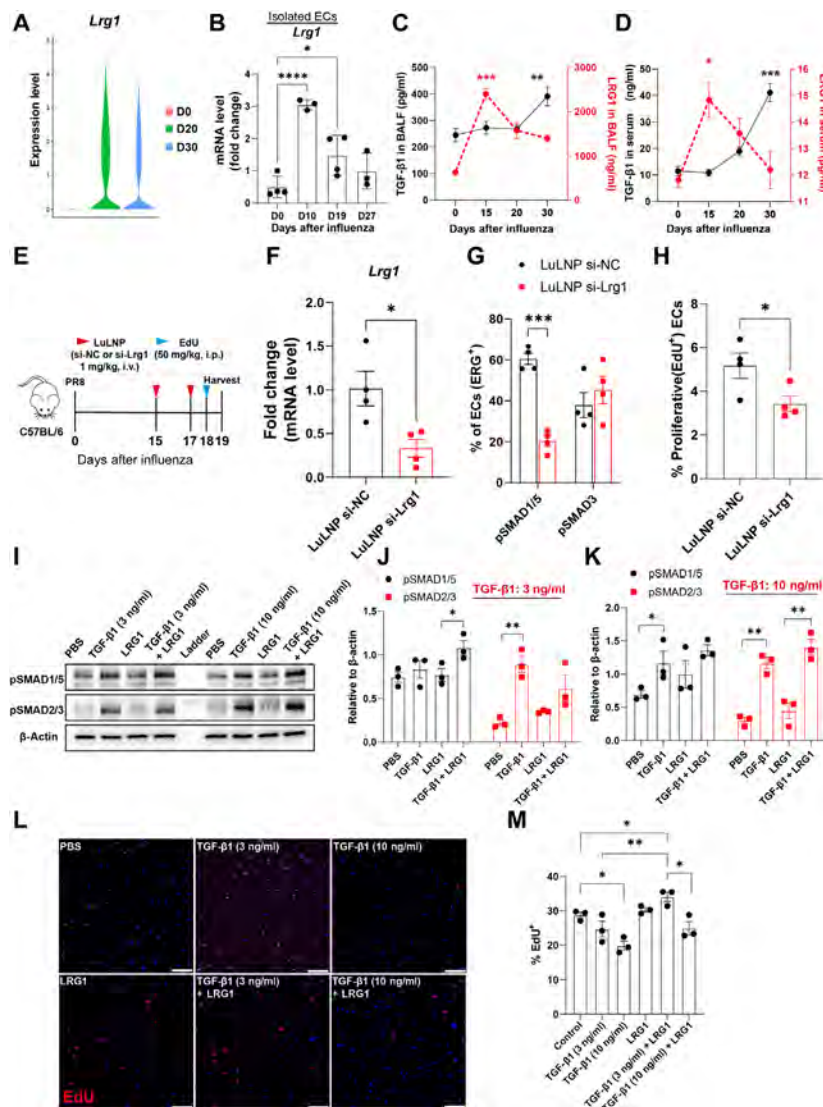
**Fig. 4. Dose-dependent effects of LRG1 and TGF-β1 regulate angiogenic proliferation.** (**A**) Violin plots of *Lrg1* mrna expression (log-normalized) in mouse lung ecs on day 0 (d0), day 20, and day 30 after influenza infection. (**B**) qPcr analysis of *Lrg1* in isolated lung ecs (cd 45⁻cd 31⁺) sorted on days 0 (uninjured), 10, 19, and 27 after influenza infection. $n = 3$ or 4 per group; data are means ± Sd, anoVa, followed by dunnett's multiple comparison test. *$P < 0.05$ and ****$P < 0.0001$ (d0 versus d10, $P < 0.0001$; d0 versus d19, $P = 0.032$). (**C** and **D**) The concentrations of active TGF-β1 (solid black line) and lrG1 (dashed red line) in BalF (c) and peripheral blood serum (d) were measured by enzyme-linked immunosorbent assay at days 0 (uninjured), 15, 20, and 30 after influenz infection. $n = 3$ or 4 per group; data are presented as means ± SeM, anoVa, followed by dunnett's multiple comparison test. *$P < 0.05$, **$P < 0.01$, and ***$P < 0.001$. TGF-β1 in BalF: d30 versus d0, $P = 0.009$; TGF-β1 in serum: d30 versus d0, $P < 0.0001$; lrG1 in BalF: d15 versus d0, $P < 0.0001$; d20 versus d0, $P = 0.004$; lrG1 in serum: d15 versus d0, $P = 0.0149$. (**E**) c57Bl6/J mice were treated with lulnPs encapsulating control noncoding sirna [si–negative control (nc), 1 mg/kg] or *Lrg1* sirna (si-*Lrg1*; 1 mg/kg) by tail-vein injection on days 15 and 18 after infection, and edU (50 mg/kg) was administered 24 hours before analysis. i.v., intravenously. (**F**) qPcr analysis of *Lrg1* in sorted ecs from mice on day 19 after infection. data are means ± SeM ($n = 4$), unpaired two-tailed *t* test, *$P = 0.0218$. (**G**) Quantific tion of SMad 1/5 and SMad 3 phosphorylation in ecs (erG⁺pSMad 1/5⁺ or erG⁺pSMad 3⁺) in mouse lungs from (e), representative images in fi. S9 (c and d). data are means ± SeM ($n = 4$), unpaired two-tailed *t* test, pSMad 1/5: ***$P < 0.0001$. (**H**) intracellular flw analysis of proliferative ecs (edU⁺) in mouse lungs from (e). data are means ± SeM ($n = 4$), unpaired two-tailed *t* test, *$P = 0.0429$. (**I**) immunoblotting analysis of indicated proteins in primary human lung ecs treated ± lrG1 (5 μg/ml) with or without low (TGF-β1$^{lo}$, 3 ng/ml) or high (TGF-β1$^{hi}$, 10 ng/ml) concentrations of TGF-β1 for 1 hour; values were quantified by densitometry, normalized to β-actin. (**J**) Quantific tion of indicated proteins in (i) of cells treated ± lrG1 with or without low concentration TGF-β1 (TGF-β1$^{lo}$). (**K**) Quantific tion of indicated proteins in (i) when cells were treated ± lrG1 combined with or without high concentration of TGF-β1 (TGF-β1$^{hi}$). data are means ± SeM ($n = 3$), unpaired two-tailed *t* test, *$P < 0.05$ and **$P < 0.01$; pSMad 1/5 in (J) lrG1 versus TGF-β1 + lr G1, $P = 0.034$; pSMad 2/3 in (J) PBS versus TGF-β1, $P = 0.0024$; pSMad 1/5 in (K) PBS versus TGF-β1, $P = 0.038$; pSMad 2/3 in (K) PBS versus TGF-β1,

$P = 0.0008$, lrG1 versus TGF-β1 + lrG1, $P = 0.0046$. (**L** and **M**) cell proliferation of primary human lung ecs treated ± lrG1 (5 μg/ml) with or without low (3 ng/ml) or high (10 ng/ml) concentrations of TGF-β1 for 6 hours, as assessed by edU incorporation assay. (l) r epresentative immunofluo escence for nuclei (blue) and edU incorporation (red). (M) Quantific tion of percentage of proliferating cells (edU⁺/daPi) in (h). data are means ± SeM ($n = 3$), anoVa, followed by dunnett's multiple comparison test. *$P < 0.05$ and **$P < 0.01$; control versus TGF-β1 (10 ng/ml), $P = 0.013$; TGF-β1 (3 ng/ml) versus TGF-β1 (3 ng/ml) + lrG1, $P = 0.0085$; control versus TGF-β1 (3 ng/ml) + lrG1, $P = 0.029$; TGF-β1 (3 ng/ml) + lrG1 versus TGF-β1 (10 ng/ml) + lrG1, $P = 0.011$.

encapsulated into LuLNPs, which were characterized by particle size, p$K_a$ (where $K_a$ is the acid dissociation constant), and mRNA encapsulation efficiency. The average diameter measured using dynamic light scattering and cryo–transmission electron microscopy for LuLNPs was 84.4 nm (fig. S12E). The ability to encapsulate mRNA evaluated by RiboGreen assays showed 87.3% encapsulation efficiency (fig. S12F). The p$K_a$ of LuLNPs, which is the pH value of LuLNP when it was 50% protonated, was 6.36 (fig. S12G), well within the range commonly used for in vivo nucleic acid delivery (*40–42*). To assess whether LuLNPs specifically targeted the lung, mice were treated with LuLNPs encapsulating luciferase mRNA (Luc-LuLNP, 0.2 mg/kg) by tail vein injection 12 hours before analysis to enable visualization of transfection efficiency using an in vivo imaging system (IVIS). Detection

of luminescence thus indicated both LNP delivery and mRNA functionality. Luciferase signal localized almost exclusively to the lung (Fig. 6A), indicating that the LuLNPs encapsulated luciferase mRNA, which was specifically expressed by lung cells. We assessed luciferase signal at 6, 24, 48, and 72 hours after Luc-LuLNP injection, observing nearly no signal by 48 hours (Fig. 6B and fig. S13A), indicating that LuLNP-delivered mRNA expression was transient. Next, oxygen saturation was assessed 24 hours after GFP LuLNP injection (0.5 mg/kg), demonstrating no obvious effects of GFP LuLNP on blood oxygenation (fig. S13B). In addition, C57BL6/J mice were administered GFP LuLNP or equal volumes of phosphate-buffered saline (PBS), and liver enzymes alanine transaminase (ALT) and aspartate transaminase (AST) were measured at 12 and 48 hours after injection. At the
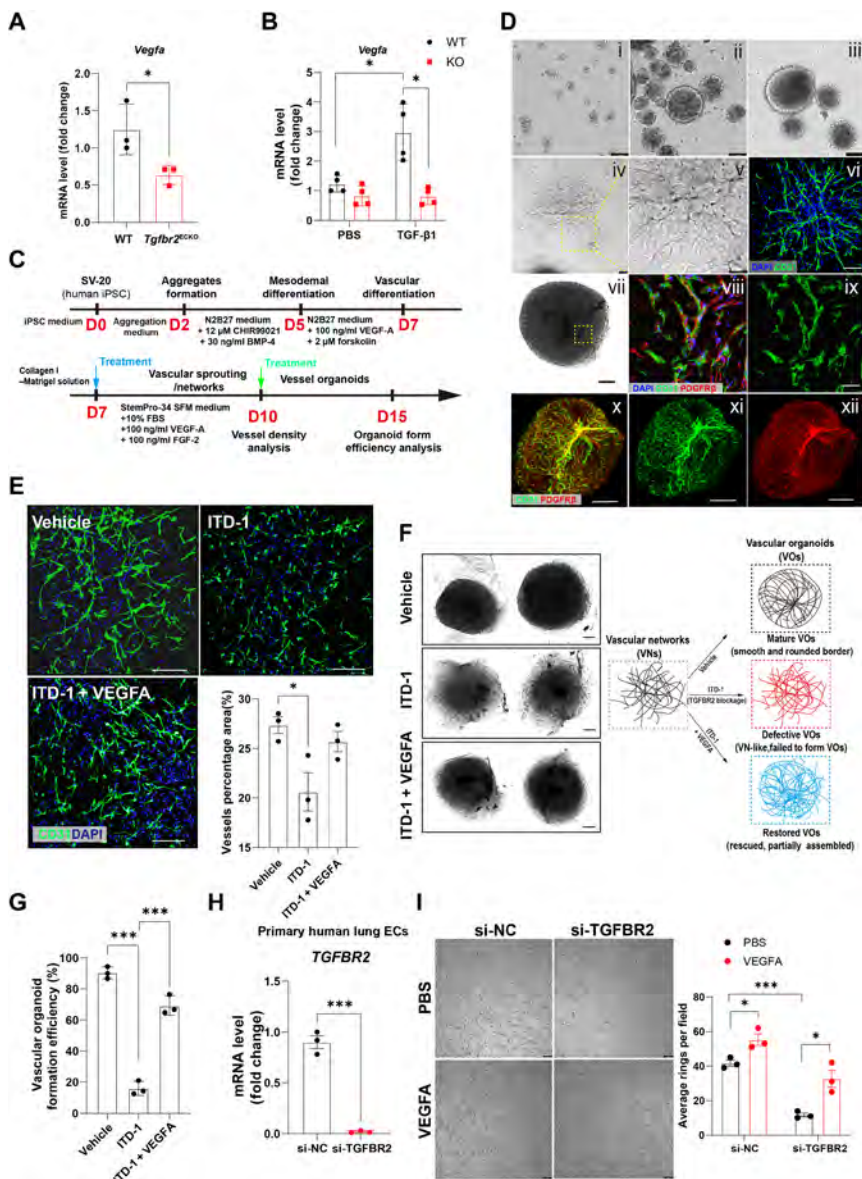
**Fig. 5. TGF-βR2 signaling induces autocrine *Vegfa* expression through SMAD activation.** (**A**) qPcr analysis of *Vegfa* in isolated lung ecs (cd 45⁻ cd 31⁺) from uninjured WT and *Tgfbr2*ecKo mice. data are means ± Sd (*n* = 3), unpaired two-tailed *t* test, *P = 0.044. (**B**) qPcr analysis showing the expression of *Vegfa* in WT and *TGFBR2*-Ko iMVecs treated ± TGF-β1 (10 ng/ml) for 24 hours. data are means ± Sd (*n* = 4), unpaired two-tailed *t* test, *P < 0.05. WT: PBS versus TGF-β1, P = 0.014; TGF-β1: WT versus Ko, P = 0.005. (**C**) Timeline for generating blood vessel organoids from hiPScs and iTd-1 treatment. For vascular network analysis, iTd-1 (10 μM) was added after vascular colony embedding into collagen i–Matrigel solution (day 7) for 3 days, with medium changed every day. For vascular organoid formation analysis, iTd-1 (10 μM) was added on day 10 when single vascular organoids were isolated from the three-dimensional (3d) matrix and then harvested on day 15, with one medium change at day 13. (**D**) images of hiPSc differentiation into vascular networks and blood vessel organoids. (i) cell aggregate formation at day 2 (d 2). Scale bar, 100 μm. (ii) cell aggregates differentiated into mesoderm (d 5). Scale bar, 100 μm. (iii) induction of mesoderm differentiation into vascular progenitor cells (d 7), before embedding into the 3d collagen i–Matrigel matrix. Scale bar, 100 μm. (iv) cell aggregates of early blood vessels grow outward in 3d collagen i–Matrigel matrix to form vascular networks (d 10). Scale bar, 100 μm. (v) higher power image of the vascular networks at day 10. Scale bar, 100 μm. (vi) immunostaining of cd 31 for ecs at day 10, cd 31 (green) and nuclei (blue). Scale bar, 100 μm. (vii) Bright field of well-formed vascular organoids at day 15. Scale bar, 200 μm. (viii) endothelial tubes (cd 31, green) in vascular organoids covered by pericytes [platelet-derived growth factor receptor beta (PdGFr β), red], nuclei (daPi, blue). (ix) immunostaining of cd 31 showing the vessel tubes in vascular organoids. Scale bar, 50 μm. (x to xii) 3d reconstruction of capillary organization (cd 31, green) in a vascular organoid covered by pericytes (PdGFr β, red) at day 15. (x) Merged, (xi) cd 31, and (xii) PdGFr β. Scale bars, 200 μm. (**E**) cell aggregates were embedded into 3d collagen i–Matrigel matrix and treated with iTd-1 (10 μg/ml), combined with or without VeGFa (100 ng/ml), or vehicle (dimethyl sulfoxide). Vascular network density was analyzed on day 3 by immunostaining of cd 31 and then quantific tion of vessels percentage area. Scale bars, 100 μm. data are presented as means ± SeM (*n* = 3), ano Va, followed by dunnett's multiple comparison test, *P < 0.05. Vehicle versus iTd-1, P = 0.029. (**F**) iTd-1 (10 μM) combined with or without VeGFa (100 ng/ml) was added on day 10 when single vascular organoid was isolated from 3d matrix and then cultured in ultralow attachment cell culture plates for 5 days. networks successfully assembled into vascular organoids with the round, smooth, and well-demarcated border. left: The representative images of fully formed vascular organoids in vehicle group and failed vascular organoids after iTd-1 treatment. right: illustration depicting the processing of vascular organoids in the left images. (**G**) The vascular organoid formation efficie y was assessed by the proportions of mature vascular organoids [Vos; as shown in (F)]. Scale bars, 200 μm. data are presented as means ± Sd (*n* = 3), ano Va, followed by dunnett's multiple comparison test, ***P < 0.001. Vehicle versus iTd-1, P < 0.0001; iTd-1 versus iTd-1 + VeGFa, P < 0.0001. (**H**) qPcr analysis of *TGFBR2* in primary human lung ecs after transfection with si-TGFBr2 (5 nM) or si-nc (5 nM) for 48 hours. data are means ± Sd (*n* = 3), unpaired two-tailed *t* test, ***P = 0.0002. (**I**) Tube formation assays of primary human lung ecs were performed 48 hours after transfection with si-*TGFBR2* (5 nM) or si-nc (5 nM). left: r epresentative images of tube networks after ecs were treated with or without VeGFa for 6 hours (20 ng/ml). right: Tube networks were quantified by counting the average rings/tubes per field under a light microscope at ×100 magnific tion. dashed circles represent vascular rings. Scale bars, 100 μm. data are means ± SeM (*n* = 3), unpaired two-tailed *t* test, *P < 0.05, **P < 0.01, and ***P < 0.001. si-nc: PBS versus VeGFa, P = 0.023; si-*TGFBR2*: PBS versus VeGFa, P = 0.015; PBS: si-nc versus si-*TGFBR2*, P = 0.00015.

standard dose (0.5 mg/kg) of GFP LuLNP, the values of AST and ALT increased slightly at 12 hours after injection but returned to normal concentrations at 48 hours after injection, similar to the PBS group (Fig. 6C and fig. S13C).

To investigate which cell types the LuLNPs transfected, mice were treated with GFP LuLNP (0.5 mg/kg) (Fig. 6D). Lungs were harvested after 18 hours for flow cytometry and immunostaining

(Fig. 6E and fig. S13D), revealing that GFP-LuLNPs yielded ~85% GFP⁺ ECs (CD45⁻/CD31⁺/GFP⁺), whereas less than 2% of any other cell type were GFP⁺ (Fig. 6F). Analysis of GFP⁺ cell distribution revealed that nearly all GFP⁺ cells were ECs (Fig. 6G). Immunostaining for CD31 showed that almost all capillary ECs were labeled by GFP, but a small number of large vascular ECs expressed little to no GFP (Fig. 6H and fig. S13E). To examine and quantify the ability

Zhao *et al.*, *Sci. Transl. Med.* **16**, eadg6229 (2024)   31 January 2024

**8 of 15**
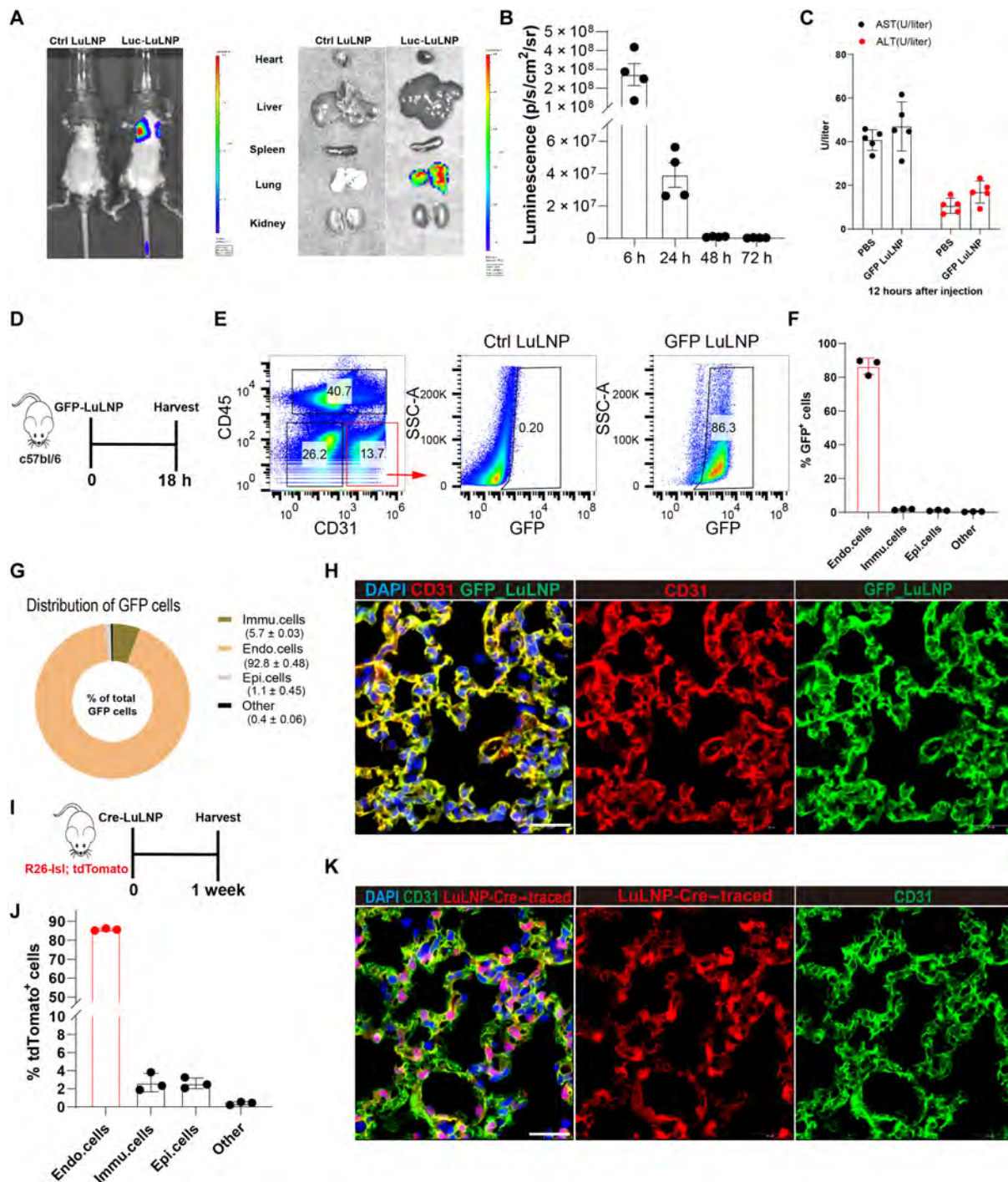
**Fig. 6. LuLNP-mediated mRNA delivery to lung ECs.** (**A**) C57Bl 6/J mice were treated with LNPs encapsulating luciferase mRNA (Luc-LNP; 0.2 mg/kg) or empty control LNPs (ctrl-LNP) by tail-vein injection 12 hours before analysis. Transfection efficiency was detected by iViS. iViS imaging of luciferase mRNA delivery to the lung (left) and heart, liver, spleen, and kidneys were dissected for luminescence imaging (right), n = 3 to 5 mice per group. (**B**) Mice were treated with Luc-LNP (0.2 mg/kg) by tail-vein injection and imaged by iViS. Quantification of luciferase signal at 6, 24, 48, and 72 hours after injection. data are means ± SeM (n = 4). (**C**) C57Bl 6/J mice were administrated LNPs encapsulating GFP mRNA (GFP LNP; 0.5 mg/kg) or equal volume of PBS, and liver enzymes aLT and aST were quantified 12 hours after injection. data are means ± SeM (n = 5). (**D**) analysis of GFP+ cells 18 hours after GFP-LNP or ctrl-LNP administration in C57Bl 6/J mice. (**E**) representative gating scheme for identification of GFP+ ecs (cd 45−/cd 31+/GFP+). (**F**) The proportion of GFP+ cells in the lung by cell type, including immune cells, ecs, epithelial cells and others (mesenchymal). data are means ± Sd (n = 3). (**G**) distribution of total GFP+ cells in each cell type. n = 3 mice. (**H**) immunostaining showing that GFP+ cells colocalize with ec marker Peca M1. Scale bar, 25 µm. (**I**) lsl-a i14-tdTomato (r 26-lsl; tdTomato) mice were administrated LNPs encapsulating cre mRNA (cre-LNP) or equal volume of vehicle empty LNPs (control) 1 week before analysis. (**J**) The proportion of LNP-cre–traced cells (tdTomato+) in the lung by cell type, including immune cells, ecs, epithelial cells, and mesenchymal ("other"). data are means ± Sd (n = 3). (**K**) immunostaining showing that LNP-cre–traced cells (tdTomato+) cells colocalize with ec marker Peca M1. Scale bar, 25 µm.

of LuLNPs to mediate lung EC-specific gene delivery/editing, tdTomato (tdTom) reporter mice were used, which expressed robust tdTom fluorescence after Cre-mediated recombination (Fig. 6I) (*43*). Cre mRNA (0.3 mg/kg) delivery by LuLNPs resulted in most capillary ECs being labeled, although, again, labeling efficiency was somewhat lower in large vessels (Fig. 6J). More than 85% of ECs were tdTom[+], with less than 5% tdTom positivity in other cell types (Fig. 6K).

To detect whether LuLNPs effectively deliver nucleic acid to the ECs during influenza injury, mice were treated with GFP LuLNP on day 17 after infection, and lungs were harvested 24 hours later (fig. S14A). Sixty percent of ECs were GFP[+], about 25% lower than in uninjured mice, but GFP was still tightly restricted to ECs (fig. S14, B and C), suggesting that LuLNPs may not be as effectively delivered to all ECs because of disruption of microvascular circulation with injury. Although vascular leakage occurs at this time point, no increase in GFP expression was observed in other cell types, indicating endothelial-specific targeting of LuLNPs even when other cell types are directly exposed. Immunostaining for CD31 further confirmed that fewer GFP[+] ECs were present in injured lung than uninjured lung (Fig. 6H and figs. S13E and S14D). Nevertheless, LuLNPs remained specific and efficient for pulmonary EC gene delivery even in an injured setting.

### LNP delivery of *Vegfa* partially restores impaired endothelial regeneration caused by endothelial TGF-βR2 deficiency

We next explored whether targeting pulmonary ECs based on LNP delivery strategies could ameliorate the exacerbation of influenza injury caused by endothelial TGF-βR2 deficiency. We initially tested delivery of mRNA encoding *Vegfa*, a well-recognized angiogenesis stimulator that is down-regulated in ECs after *Tgfbr2* deletion, to uninjured wild-type (WT) mice. qPCR of sorted ECs demonstrated increased *Vegfa* expression 24 hours after *Vegfa* LuLNP administration (fig. S15A). Histopathology and immunostaining demonstrated that *Vegfa* overexpression by LuLNPs in lung ECs did not cause overt vascular morphology abnormalities or local inflammation (fig. S15, B and C). In addition, mice were treated with PBS, GFP LuLNP or LuLNP (0.5 mg/kg) (without encapsulated mRNA) by tail vein injection, and the total number of cells in BALF and numbers of immune cells (CD45^{+}) in the BALF were evaluated at 24 and 72 hours after injection. Twenty-four hours after LuLNP injection, the numbers of total and CD45^{+} cells in the GFP LuLNP group increased slightly although not significantly ($P > 0.05$; fig. S15, D and E) and returned to baseline by 72 hours. VEGFA is also known to increase vascular permeability (*44*) that can directly contribute to pulmonary edema (*45*). We therefore assessed vascular permeability after administration of escalating consecutive doses of *Vegfa* LuLNP (0.5 mg/kg, every 24 hours, intravenously). Vascular leakage was observed only after the administration of five consecutive doses as judged by total protein concentration and dextran in the BALF (fig. S15, F and G).

To determine whether LuLNP delivery of *Vegfa* rescued endothelial proliferation loss due to TGF-βR2 deficiency, WT and *Tgfbr2*[ECKO] mice were treated with control or *Vegfa* LuLNP (0.5 mg/kg) on day 15 after infection, and samples were collected 72 hours later. To prevent the mild inflammation caused by LNP injection, dexamethasone (DEX) was injected intraperitoneally (i.p.) 30 min before LuLNP injection (*46*) in all mice (Fig. 7A). The concentration of VEGFA in the BALF increased after 24 hours of *Vegfa* LuLNP treatment (fig. S15H). Flow analysis demonstrated that *Vegfa* LuLNP enhanced proliferation of ECs in *Tgfbr2*[ECKO] mice, supporting the

notion that VEGFA is an important downstream effector of TGF-βR2 signaling in this model, whereas proliferation increases in WT mice were not statistically significant ($P > 0.05$; Fig. 7B). Immunofluorescence analysis of proliferating ECs based on nuclear coexpression of Ki67 with endothelial-specific transcription factor ERG [erythroblast transformation-specific (ETS)–related gene] (*8*, *33*) confirmed increased endothelial proliferation in *Vegfa* LuLNP lungs 18 days after infection (Fig. 7C). Because VEGFA protects against apoptosis, prolonging cell survival (*47*, *48*), we quantified apoptotic ECs in lungs from both WT and *Tgfbr2*[ECKO] mice treated with *Vegfa* LuLNP or Ctrl LuLNP by TUNEL flow cytometry (fig. S15I). LuLNP delivery of *Vegfa* imparted obvious protection against endothelial apoptosis in all mice (Fig. 7D) but to a higher degree in *Tgfbr2*[ECKO] mice. This effect extended beyond direct effects on ECs because we observed a similar reduction in apoptosis in surrounding non-ECs as well, further implicating vascular repair as a critical component for effective whole-organ regeneration (Fig. 7E).

To investigate whether endothelial overexpression of *Vegfa* by LuLNPs accelerated the recovery of lung function, especially the deterioration caused by endothelial deletion of TGF-βR2 during influenza injury, WT and *Tgfbr2*[ECKO] mice were treated with control or *Vegfa* LuLNP on days 15 and 21 after influenza infection, and lungs were harvested on day 27 (Fig. 7F). *Vegfa* LuLNP treatment increased blood oxygen saturation and improved body weight recovery specifically in *Tgfbr2*[ECKO] mice compared with the Ctrl LuLNP group (Fig. 7, G and H). In addition, *Tgfbr2*[ECKO] mice treated with *Vegfa* LuLNP showed reduced lung inflammation as indicated by lower total protein concentration and MPO activity in the BALF (Fig. 7, I and J), as well as decreased damage, remodeling, and higher vessel density (Fig. 7, K to P). However, the therapeutic efficacy of *Vegfa* LuLNP treatment in WT mice was not as pronounced as in *Tgfbr2*[ECKO] mice (fig. S15, J to M), emphasizing the sufficiency of EC-derived VEGFA in supporting vascular repair processes when TGF-βR2 signaling is intact. Furthermore, excessive angiogenesis might contribute to the progression of fibrosis (*49*). However, Vegfa LNP treatment did not promote lung fibrosis during viral injury as judged by collagen I staining (fig. S15N).

We also asked whether endothelial overexpression of *Tgfbr2* could rescue the vascular endothelial repair impairment in *Tgfbr2*[ECKO] mice. DEX was injected intraperitoneally 30 min before LuLNPs injection in WT and *Tgfbr2*[ECKO] mice, and then all mice were treated with *Tgfbr2* LuLNP (0.5 mg/kg) or control LuLNP (0.5 mg/kg) on days 15 and 20 after infection, followed by EdU treatment every other day (fig. S16A). *Tgfbr2* LuLNP treatment was unable to completely restore CAR4^{+} aerocytes caused by endothelial *Tgfbr2* deficiency (fig. S16, B and C). However, it did enhance EC proliferation in both groups (fig. S16, D and E). Furthermore, because TGF-βR2 serves as a receptor for TGF-β1, we explored whether recombinant TGF-β1 protein could promote lung endothelial repair during influenza-induced lung injury. C57BL/6 mice were treated with recombinant TGF-β1 (100 μg/kg, i.p.) every other day from day 7 after infection and accompanied by EdU treatment (fig. S16F). Administration of recombinant TGF-β1 did not lead to any observable increase in EC proliferation or quantity (fig. S16, G and H).

### DISCUSSION

Our previous work revealed that regenerated ECs upon influenza injury mainly arise from proliferation of preexisting ECs, and myriad

Zhao et al., Sci. Transl. Med. **16**, eadg6229 (2024)    31 January 2024

**10 of 15**
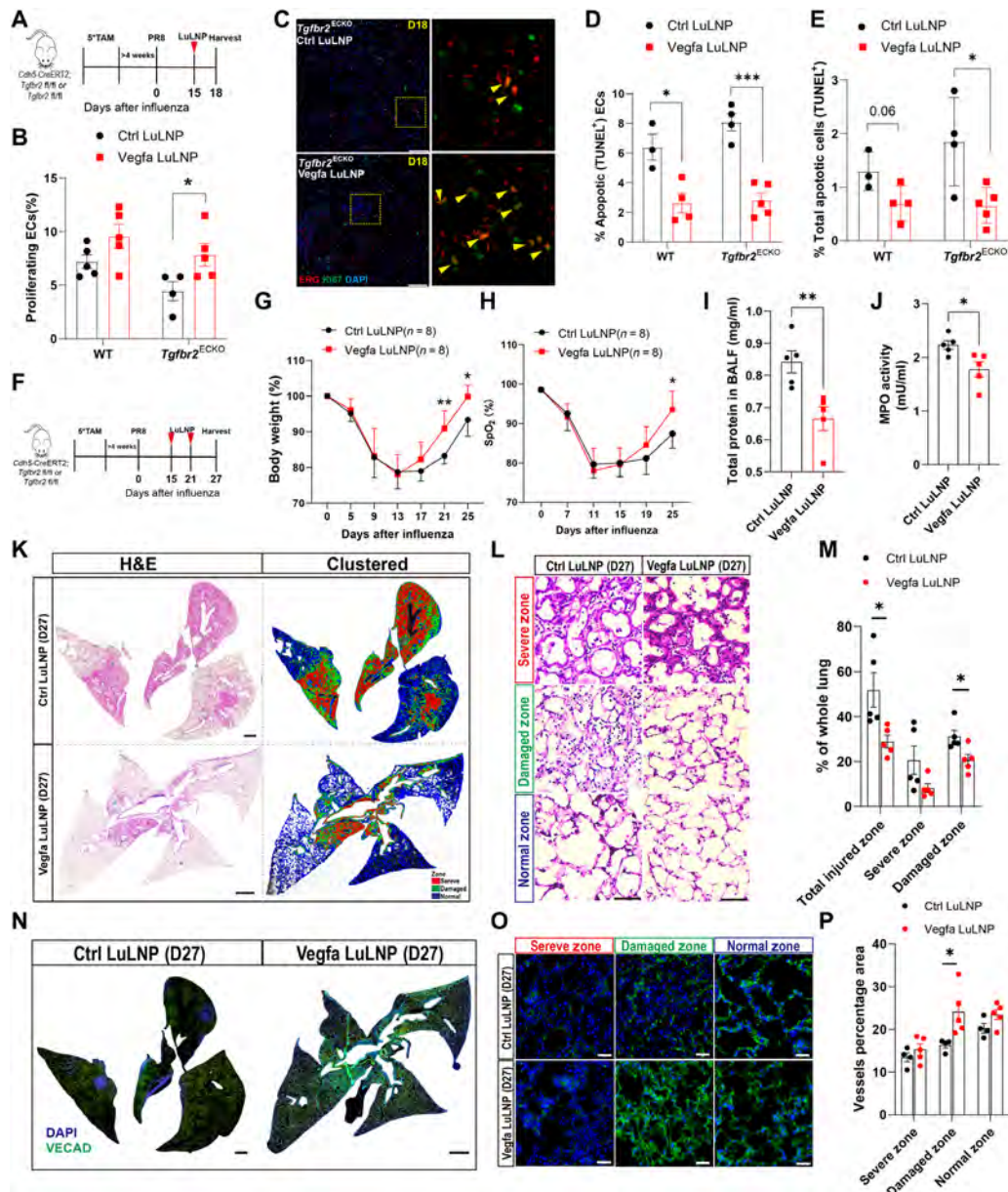
**Fig. 7. LuLNP delivery of *Vegfa* mRNA alleviates the exacerbation of influenza injury caused by endothelial *Tgfbr2* deficiency.** (**A**) Timeline for l uln P administration and sampling. WT and *Tgfbr2*ecKo mice were treated with empty l uln Ps (c trl l uln P) or l uln Ps encapsulating *Vegfa* mrna (*Vegfa* l uln P) (0.5 mg/kg) on day 15 after infection, and samples were collected after 72 hours. d examethasone-21-phosphate (deX) was injected i.p. (2 mg/kg) into the mice 30 min before l uln P injection in all mice. (**B**) intracellular fl w cytometry quantific tion of proliferative ec s (cd 31+/Ki67+) 72 hours after administration of control or *Vegfa* l uln Ps in lung ec s from WT and *Tgfbr2*ecKo mice. data are means ± SeM (*n* = 5), unpaired two-tailed *t* test, *P < 0.05. *Tgfbr2*ecKo: c trl l uln P versus *Vegfa* l uln P, P = 0.048. (**C**) r epresentative immunostaining of proliferative ec s 72 hours after administration of control or *Vegfa* l uln P in *Tgfbr2*ecKo mice lungs. Scale bars, 100 μm. (**D** and **E**) Quantific tion of apoptotic (TUnel +) ec s (d) and total apoptotic cells (e). *n* = 3 to 5 per group. data are means ± SeM, unpaired two-tailed *t* test, *P < 0.05 and ***P < 0.001. (d) WT: c trl l uln P versus *Vegfa* l uln P, P = 0.018; *Tgfbr2*ecKo: c trl l uln P versus *Vegfa* l uln P, P = 0.0002. (e) WT: c trl l uln P versus *Vegfa* l uln P, P = 0.06; *Tgfbr2*ecKo: c trl l uln P versus *Vegfa* l uln P, P = 0.02. (**F**) Timeline for indicated l uln P administration and sampling. WT and *Tgfbr2*ecKo mice were treated with c trl l uln P or *Vegfa* l uln P (0.5 mg/kg) on days 15 and 21 after infection, and lungs were harvested on day 27. deX was injected i.p. (2 mg/kg) into the mice 30 min before l uln Ps injection in all mice. (**G** and **H**) Body weight (G) and capillary oxygen saturation (h) for ln P-treated *Tgfbr2*ecKo mice. data are means ± Sd (*n* = 8), unpaired two-tailed *t* test, *P < 0.05 and **P < 0.01. (G) d21: c trl l uln P versus *Vegfa* l uln P, P = 0.0013; d25: c trl l uln P versus *Vegfa* l uln P, P = 0.04. (h) d25: c trl l uln P versus *Vegfa* l uln P, P = 0.011. (**I** and **J**) Total protein (i) and MPo activity (J) were quantified in Bal F collected from *Tgfbr2*ecKo mice that received c trl l uln P or *Vegfa* l uln P treatment and harvested at day 27 after infection. data are means ± SeM (*n* = 5), unpaired two-tailed *t* test, *P < 0.05 and **P < 0.01. (i) P = 0.008; (J) P = 0.023. (**K** to **P**) *Tgfbr2*ecKo mice received c trl l uln P or *Vegfa* l uln P treatment, and lung samples were harvested on day 27 after infection. (K) l eft: Tile scan images of h &e stain; demarcated boxes indicate different injury zones. r ight: c lustered injury zone maps produced from left h &e images. Scale bars, 1 mm. (l ) Zoomed-in images from the demarcated boxes area in (K). Scale bars, 50 μm. (M) Quantific tion of injury area in different injury zones in (K). (n) Tile scan images of immunostaining of vascular endothelial cadherin (Vecad ). Scale bars, 1 mm. (o) images of Vecad staining in differ-ent injury zones in (n). Scale bars, 25 μm. (P) Quantific tion of vessel percentage judged by Vecad staining in different injury zones in (n). data are means ± SeM (*n* = 5), unpaired two-tailed *t* test, *P < 0.05. (M) c trl l uln P versus *Vegfa* l uln P: total injured zone, P = 0.023; damaged zone, P = 0.022. (P) c trl l uln P versus *Vegfa* l uln P: damaged zone, P = 0.03.

signals and pathways are needed for effective vascular repair. Our work here identifies one such pathway, highlighting up-regulation of TGF-βR2 and other TGF-β pathway components in human and mouse ECs upon viral lung injury, including activation of SMAD1/5/8, implicating TGF-β pathway activity in lung vascular repair. We confirmed the functional requirement for this pathway by demonstrating that mice with endothelial deletion of *Tgfbr2* exhibit a failure to effectively regenerate the lung endothelium, thus increasing mortality and prolonging morbidity.

TGF-β signaling is a complex and nuanced pathway. In ECs from other tissues, TGF-β activation of SMAD2/3 is typically angiostatic, whereas SMAD1/5/8 is angiogenic, so it is difficult to predict how ECs will respond to a given TGF-β ligand/receptor agonist. LRG1, a secreted glycoprotein, is known to direct EC TGF-β signaling toward the SMAD1/5/8 proangiogenic pathway (*36, 50*). Critically, we observed autocrine EC up-regulation of LRG1 that slowly normalizes as injury resolves. Treatment with exogenous LRG1 or LRG1 overexpression imparted angiogenic properties on ECs, whereas LRG1 knockdown in vivo reduced EC proliferation and SMAD1/5 activation, a finding further supported by previous studies demonstrating direct interaction of LRG1 with TGF-βR2 (*36*). On the basis of this evidence, we propose the following model: First, in the angiogenic proliferation and migration stage (10 to 20 days after infection), up-regulation of LRG1 drives angiogenesis by shunting TGF-β signaling toward angiogenic SMAD1/5/8 (fig. S17). Then, at later time points when vascular proliferation is essentially completed, EC *Lrg1* expression is also reduced, allowing classical TGF-β signaling in the newly generated ECs to promote luminalization and maturation to establish functional blood vessels. At these later time points, TGF-β likely promotes angiostatic SMAD2/3, antagonizing any remaining LRG1-induced EC proliferation to prevent abnormal angiogenesis (*36, 51*). Although we demonstrated that LRG1/TGF-β signaling is critical for lung EC repair, we note that *Tgfbr2* deletion is not uniformly lethal and some mice do still recover from infection, albeit slowly, reinforcing the involvement of additional yet-to-be-identified angiogenic signaling pathways.

Recognizing that lung endothelium is a critical target for delivery of therapeutic molecules or genes for recovery from ARDS, we demonstrated that *Vegfa* mRNA administration protected ECs and other lung cells from apoptosis, indicating that effective endothelial repair promotes holistic recovery of the entire tissue (*47, 48*). Although vascular-directed gene therapy holds great promise, VEGFA is also well known to increase vascular permeability (*44*) and pulmonary edema (*45*), and similar to LRG1, VEGFA overexpression can induce pathological angiogenesis (*52*). As such, other vascular repair genes, such as *Stat3* (*16*) and *Foxm1* (*53*), may ultimately be better suited for endothelial gene therapy than *Vegfa*, especially because VEGFA does not appear to be limiting in animals with intact TGF-βR2 (fig. S15, J to M). Furthermore, some LNPs are capable of causing transient inflammatory storms (*46*) with a risk of exacerbating disease, so clinical use of LNP-based therapies in diseased patients will require extra care and possibly combinatorial treatment with anti-inflammatory agents.

This work both identifies a role for TGF-β signaling in lung vascular repair and highlights potential nanomedicine approaches to enhancing angiogenic regeneration, but there are limitations to our study. We did not identify the initiating signal(s) that up-regulate TGF-βR2 in ECs early after infection. Given the robust innate and adaptive immune responses that occur after viral infection, we predict that endothelial TGF-βR2 up-regulation is likely induced by inflammatory signals such as interferons and alarmins. Further, although previous studies indicated that gCaps are likely the most relevant facultative progenitor cells, our studies did not assess whether the impaired regeneration phenotype is due entirely to TGF-β signaling in gCaps or whether it is also important in other EC types. Last, it will be important to evaluate whether TGF-βR2 signaling is important in other injury contexts, including sterile injuries such as aspiration pneumonia or chronic conditions including emphysema and chronic obstructive pulmonary disease (COPD). In summary, our studies further highlight the importance of vascular endothelial repair after severe viral lung injury, provide insights into TGF-β signaling as an essential pathway for effective repair, and suggest the potential for endothelial-targeted gene therapy using next-generation approaches for treating critically ill patients.

## MATERIALS AND METHODS
### Study design
The objective of this study was to investigate lung vascular injury and underlying repair mechanisms during viral pneumonia using an influenza virus–induced lung injury mouse model. For in vivo studies, experimental and control animals are specifically described as such in Results and figure legends. Control mice for in vivo *Tgfbr2* deletion experiments (*Tgfbr2*$^{ECKO}$) were an approximately equal mix of *Tgfbr2*$^{flox/flox}$ mice lacking Cre and VECAD$^{CreERT2}$ (*Cdh5*$^{CreERT2}$) mice bearing only WT *Tgfbr2* alleles. Control animals were always treated identically including the same dosing of tamoxifen (see below). For in vitro studies, the experimental samples were *TGFBR2* KO or *LRG1* overexpression iMVECs, human iPSCs (SV-20), SV-20–derived vascular organoids, and human lung primary ECs transfected with si-TGFBR2 (*TGFBR2* siRNA), treated with indicated molecules. Control samples were the corresponding empty vector–transduced iMVECs and/or vehicle-treated (dimethyl sulfoxide or PBS depending on the reagent) iMVECs/human primary lung ECs/SV-20–derived vascular organoids or human lung primary ECs transfected with siRNA negative control (si-NC). Sample size was determined by availability and previous experience with influenza infection experiments in mice. No outliers were excluded from the study. A minimum of three animals per group was used for studies involving statistical analyses, and the *n* for individual experiments is indicated in the figure legends. Blinding was performed during data collection and analysis when possible, given the survival and body weight loss differences in treated and untreated groups. For each experiment, sample size reflects the number of independent biological replicates.

### Participants and ethical compliance
The normal, healthy control samples used for this study were from deidentified nonused lungs donated for organ transplantation by an established protocol [Prospective Registry of Outcomes in Patients Electing Lung Transplantation (PROPEL), approved by University of Pennsylvania Institutional Review Board] with informed consent in accordance with institutional and National Institutes of Health (NIH) procedures. Consent was provided by next of kin or health care proxy. Diseased tissue was obtained from participants enrolled at the University of Pennsylvania as part of the PROPEL (Penn cohort). All selected patients had a history of COVID infection based on PCR testing that resulted in respiratory failure and required lung transplantation based on current guidelines but tested negative by PCR multiple times before tissue acquisition. The institutional review

Zhao *et al.*, *Sci. Transl. Med.* **16**, eadg6229 (2024)   31 January 2024

**12 of 15**

board of the University of Pennsylvania approved this study, and written informed consent was obtained from all participants before inclusion in the study. All patient information was removed before use. This use does not meet the current NIH definition of human individual research, but all relevant guidelines and regulations and all institutional procedures required for human individual research were followed throughout the reported experiments.

## Animals and treatments

*Tgfbr2*[flox] mice (31) (Jackson Laboratory stock #012603) were crossed with VECAD[CreERT2] (*Cdh5*[CreERT2]) mice (54) to produce VECAD[CreERT2]; *Tgfbr2*[flox/flox] mice. VECAD[CreERT2]; *Tgfbr2*[flox/flox] mice and controls (mice bred in parallel either lacking VECAD[CreERT2] or *Tgfbr2*[flox/flox]) were administered five doses of tamoxifen (0.25 mg/g of body weight) in 50 μl of corn oil every other day and rested for 3 to 5 weeks after the last injection, resulting in EC-specific deletion of *Tgfbr2* in adult mice (*Tgfbr2*[ECKO]). Afterward, influenza virus A/H1N1/PR/8 was administered intranasally at 50 to 60 TCID50 (50% tissue culture infectious dose) units to mice as previously described (8, 55). Mice were weighed regularly and euthanized at the indicated time points for tissue harvest. In this study, all mice were used at 6 to 8 weeks old, and mice of both sexes were used in equal proportions.

## Synthesis of lung-targeted ionizable lipid and formulation into LNPs (LuLNPs)

Lung-targeted ionizable lipid—$N^1,N^{19}$-didodecyl-4,7,13,16-tetrakis(3-(dodecylamino)-3-oxopropyl)-9,9,11,11-tetramethyl-10-oxa-4,7,13,16-tetraaza-9,11-disilanonadecanediamide—was synthesized through Michael-addition reaction (synthetic details in fig. S12, A and B). Briefly, 1,3-bis(2-aminoethylaminomethyl)tetramethyldisiloxane (0.278 g, 1 mmol, 1 equiv) and *N*-dodecylacrylamide (1.72 g, 7.2 mmol, 7.2 equiv) were added in a glass vial equipped with a stir bar dissolved in ethanol. The reaction was stirred at 80°C for 3 days. The final product was purified by CombiFlash Rf-200i chromatography to afford a yellowish solid.

Lung-targeted ionizable lipid: $^1$H nuclear magnetic resonance (400 MHz, MeOD), δ 3.23 to 3.13 (m, 12H), 2.92 to 2.70 (m, 12H), 2.66 to 2.50 (m, 8H), 2.48 to 2.33 (m, 12H), 2.31 to 2.25 (s, 4H), 1.62 to 1.23 (m, 120H), 0.99 to 0.88 (m, 18H), 0.16 (s, 12H). Liquid chromatography–mass spectrometry (mass/charge ratio): calculated for [M + H]+: 1715.9, found: 1715.5.

LuLNPs were formulated according to our previous study (41). Briefly, an ethanol phase containing all lipids and an aqueous phase containing mRNA [Luc mRNA, Cre mRNA, enhanced GFP (EGFP) mRNA, and Vegfa mRNA] were mixed using a microfluidic device to formulate LNPs. The ethanol phase contained lipidoids (synthetic details in fig. S12, C and D), 1,2-dioleoyl-*sn*-glycero-3-phosphoethanolamine (AvantiPolarLipids), cholesterol, and 1,2-dimyristoyl-*sn*-glycero-3-phosphoethanolamine-*N*-[methoxy(polyethyleneglycol)-2000] (C14-PEG2000; AvantiPolarLipids) with a fixed molar ratio of 35, 16, 46.5, and 2.5%, respectively. Aqueous phase was composed of mRNA dissolved in 10 mM citrate buffer. The ethanol and aqueous phases were mixed at a flow rate of 1.8 and 0.6 ml/min (3:1) using Pump33DS syringe pumps. LNPs were dialyzed in 1× PBS using a microdialysis cassette (20,000 molecular weight cutoff; Thermo Fisher Scientific) for 2 hours and then filtered through a 0.22-μm filter. Zetasizer Nano was used to measure the *Z*-average diameters, polydispersity index, and zeta potential. mRNA concentration and encapsulation efficiency in each LNP formulation were measured using a modified Quant-iT RiboGreen (Thermo Fisher

Scientific) assay on a plate reader. LuLNP characterization including hydrodynamic diameter, p$K_a$ value, and encapsulation efficiency was performed as described previously (41).

For in vivo delivery of LuLNPs, mice were administered with LuLNPs encapsulating mRNAs/siRNAs [Cre mRNA, 0.3 mg/kg (TriLink Biotechnology, #L-7211); luciferase mRNA, 0.2 mg/kg; EGFP mRNA, 0.5 mg/kg; mouse *Vegfa* and *Tgfbr2* mRNA, 0.5 mg/kg, were provided by D. Weissman laboratory, negative control siRNA (si-NC, #AM4635) and *Lrg1* siRNA (si-Lrg1, #4390816; 1 mg/kg), purchased from Thermo Fisher Scientific] or equal volume of vehicle control empty LuLNPs by tail-vein injection depending on experimental conditions. Luciferase expression was evaluated using an IVIS Spectrum imaging system (Caliper Life Sciences) 12 hours after injection. Ex vivo imaging was performed on the heart, liver, spleen, lung, and kidney after resection. All animal experiments were carried out under the guidelines set by the University of Pennsylvania's Institutional Animal Care and Use Committees and followed all NIH Office of Laboratory Animal Welfare regulations.

## Statistical analysis

All statistical calculations were performed using GraphPad Prism 9. All in vitro experiments were repeated at least three times unless otherwise stated. Unpaired two-tailed Student's *t* tests were used to ascertain statistical significance between two groups. One-way analysis of variance (ANOVA) was used to assess statistical significance between three or more groups with one experimental parameter. For details on statistical analyses, tests used, size of *n*, definition of significance, and summaries of statistical outputs, see corresponding figure legend and Results.

## Image analysis

For quantitative images in this study, four to six images were taken randomly from each sample/section on a Leica Dmi8 microscope, a Leica SP5-FLIM inverted confocal microscope, or Zeiss LSM 710 confocal microscope. Immunostainings of Fig. 1E and fig. S15N were quantified by mean gray value using ImageJ software. The quantification of hematoxylin and eosin (H&E) sections (Figs. 2, J to L, and 7, K to M) was performed by scanning the whole lung under 4× objective using LAS X tile scan mode and quantified by a previously described unbiased computational imaging approach (32). The vessels densities per percentage in Figs. 2 (N and O), 5E, and 7 (O and P) and fig. S5C were quantified by AngioTool (56). Western blot bands in Fig. 4I and fig. S8 (B, E, and G) were quantified by ImageJ software. Cell counts in Fig. 4L and fig. S1B were counted manually using LAS X software (Leica). Images of Fig. 5 (F, G, and I) and figs. S8I, S9 (B and C), S10 (C and D), and S15C were obtained and quantified manually using LAS X (Leica). Luciferase signaling in fig. S13A was quantified by an IVIS imaging system (PerkinElmer).

## Supplementary Materials

**This PDF file includes:**
Materials and Methods
Figs. S1 to S17
Table S1

**Other Supplementary Material for this manuscript includes the following:**
data file S
Mdar reproducibility checklist

# REFERENCES AND NOTES

1. G. Grasselli, T. Tonetti, a. Protti, T. langer, G. Girardis, G. Bellani, J. laffey, G. carrafiell, l. carsana, c. rizzuto, a. Zanella, V. Scaravilli, G. Pizzilli, d. l. Grieco, l. di Meglio, G. de Pascale, e. lanza, F. Monteduro, M. Zompatori, c. Filippini, F. locatelli, M. cecconi, r. Fumagalli, S. nava, J. l. Vincent, M. antonelli, a. S. Slutsky, a. Pesenti, V. M. ranieri, on behalf of the collaborators, Pathophysiology of coVid-19-associated acute respiratory distress syndrome: a multicentre prospective observational study. *Lancet Respir. Med.* **8**, 1201–1208 (2020).

2. M. J. hsieh, W. c. lee, h. Y. cho, M. F. Wu, h. c. hu, K. c. Kao, n. h. chen, Y. h. Tsai, c. c. huang, recovery of pulmonary functions, exercise capacity, and quality of life after pulmonary rehabilitation in survivors of ardS due to severe influenza a (h1n1) pneumonitis. *Influenza Other Respir. Viruses* **12**, 643–648 (2018).

3. J. d. crapo, b. e. Barry, P. Gehr, M. Bachofen, e. r. Weibel, cell number and cell characteristics of the normal human lung. *Am. Rev. Respir. Dis.* **126**, 332–337 (1982).

4. n. S. Mangalmurti, J. P. reilly, d. B. cines, n. J. Meyer, c. a. hunter, a. e. Vaughan, coVid-19-associated acute respiratory distress syndrome clarified: a vascular endotype? *Am. J. Respir. Crit. Care Med.* **202**, 750–753 (2020).

5. a. huertas, d. Montani, l. Savale, J. Pichon, l. Tu, F. Parent, c. Guignabert, M. humbert, endothelial cell dysfunction: a major player in SarS-coV-2 infection (coVid-19)? *Eur. Respir. J.* **56**, 2001634 (2020).

6. J. r. Teijaro, K. B. Walsh, S. cahalan, d. M. Fremgen, e. roberts, F. Scott, e. Martinborough, r. Peach, M. B. a. oldstone, h. rosen, endothelial cells are central orchestrators of cytokine amplific tion during influenza virus in ection. *Cell* **146**, 980–991 (2011).

7. T. K. niethamer, c. T. Stabler, J. P. leach, J. a. Zepp, M. P. Morley, a. Babu, S. Zhou, e. e. Morrisey, defining the ole of pulmonary endothelial cell heterogeneity in the response to acute lung injury. *eLife* **9**, e53072 (2020).

8. G. Zhao, a. i. Weiner, K. M. neupauer, M. F. de Mello costa, G. Palashikar, S. adams-Tzivelekidis, n. S. Mangalmurti, a. e. Vaughan, regeneration of the pulmonary vascular endothelium after viral pneumonia requires coUP-TF2. *Sci. Adv.* **6**, eabc4493 (2020).

9. c. e. evans, M. l. iruela-arispe, Y. Y. Zhao, Mechanisms of endothelial regeneration and vascular repair and their application to regenerative medicine. *Am. J. Pathol.* **191**, 52–65 (2021).

10. M. J. Goumans, Z. liu, P. ten dijke, TGF-β signaling in vascular biology and dysfunction. *Cell Res.* **19**, 116–127 (2009).

11. M. J. Goumans, G. Valdimarsdottir, S. itoh, a. rosendahl, P. Sideras, P. ten dijke, Balancing the activation state of the endothelium via two distinct TGF-β type i receptors. *EMBO J.* **21**, 1743–1753 (2002).

12. S. P. oh, T. Seki, K. a. Goss, T. imamura, Y. Yi, P. K. donahoe, l. li, K. Miyazono, P. ten dijke, S. Kim, e. li, activin receptor-like kinase 1 modulates transforming growth factor-β 1 signaling in the regulation of angiogenesis. *Proc. Natl. Acad. Sci. U.S.A.* **97**, 2626–2631 (2000).

13. M. J. Goumans, F. lebrin, G. Valdimarsdottir, controlling the angiogenic switch. *Trends Cardiovasc. Med.* **13**, 301–307 (2003).

14. M. oshima, h. oshima, M. M. Taketo, TGF-β receptor type ii deficien y results in defects of yolk sac hematopoiesis and vasculogenesis. *Dev. Biol.* **179**, 297–302 (1996).

15. h.-l. nguyen, Y. J. lee, J. Shin, e. lee, S. o. Park, J. h. Mccarty, S. P. oh, TGF-β signaling in endothelial cells, but not neuroepithelial cells, is essential for cerebral vascular development. *Lab. Invest.* **91**, 1554–1563 (2011).

16. F. Sun, G. Wang, a. Pradhan, K. Xu, J. Gomez-arroyo, Y. Zhang, G. T. Kalin, Z. deng, r. J. Vagnozzi, h. he, a. W. dunn, Y. Wang, a. J. York, r. S. hegde, J. c. Woods, T. V. Kalin, J. d. Molkentin, V. V. Kalinichenko, nanoparticle delivery of STaT3 alleviates pulmonary hypertension in a mouse model of alveolar capillary dysplasia. *Circulation* **144**, 539–555 (2021).

17. a. W. dunn, V. V. Kalinichenko, d. Shi, highly effici t in vivo targeting of the pulmonary endothelium using novel modific tions of polyethylenimine: an importance of charge. *Adv. Healthc. Mater.* **7**, e1800876 (2018).

18. X. Zhang, h. Jin, X. huang, B. chaurasiya, d. dong, T. P. Shanley, Y. Y. Zhao, robust genome editing in adult vascular endothelium by nanoparticle delivery of criSPr-cas9 plasmid dna. *Cell Rep.* **38**, 110196 (2022).

19. K. l. Swingle, a. G. hamilton, M. J. Mitchell, lipid nanoparticle-mediated delivery of mrna therapeutics and vaccines. *Trends Mol. Med.* **27**, 616–617 (2021).

20. a. akinc, M. a. Maier, M. Manoharan, K. Fitzgerald, M. Jayaraman, S. Barros, S. ansell, X. du, M. J. hope, B. l. Mui, S. c. Semple, Y. K. Tam, M. ciufolini, d. Witzigmann, J. a. Kulkarni, r. van der Meel, P. r. cullis, The onpattro story and the clinical translation of nanomedicines containing nucleic acid-based drugs. *Nat. Nanotechnol.* **14**, 1084–1087 (2019).

21. X. hou, T. Zaks, r. langer, Y. dong, lipid nanoparticles for mrna delivery. *Nat. Rev. Mater.* **6**, 1078–1094 (2021).

22. X. han, h. Zhang, K. Butowska, K. l. Swingle, M.-G. alameh, d. Weissman, M. J. Mitchell, an ionizable lipid toolbox for rna delivery. *Nat. Commun.* **12**, 7233 (2021).

23. J. G. rurik, i. Tombacz, a. Yadegari, P. o. M. Fernandez, S. V. Shewale, l. li, T. Kimura, o. Y. Soliman, T. e. Papp, Y. K. Tam, B. l. Mui, S. M. albelda, e. Pure, c. h. June, h. aghajanian, d. Weissman, h. Parhiz, J. a. epstein, car T cells produced in vivo to treat cardiac injury. *Science* **375**, 91–96 (2022).

24. Q. cheng, T. Wei, l. Farbiak, l. T. Johnson, S. a. dilliard, d. J. Siegwart, Selective organ targeting (SorT) nanoparticles for tissue-specific rna delivery and criSPr-cas gene editing. *Nat. Nanotechnol.* **15**, 313–320 (2020).

25. a. akinc, a. Zumbuehl, M. Goldberg, e. S. leshchiner, V. Busini, n. hossain, S. a. Bacallado, d. n. nguyen, J. Fuller, r. alvarez, a. Borodovsky, T. Borland, r. constien, a. de Fougerolles, J. r. dorkin, K. narayanannair Jayaprakash, M. Jayaraman, M. John, V. Koteliansky, M. Manoharan, l. nechev, J. Qin, T. racie, d. raitcheva, K. G. rajeev, d. W. Sah, J. Soutschek, i. Toudjarska, h. P. Vornlocher, T. S. Zimmermann, r. langer, d. G. anderson, a combinatorial library of lipid-like materials for delivery of rnai therapeutics. *Nat. Biotechnol.* **26**, 561–569 (2008).

26. S. liu, Q. cheng, T. Wei, X. l. Yu, l. T. Johnson, l. Farbiak, d. J. Siegwart, Membrane-destabilizing ionizable phospholipids for organ-selective mrna delivery and criSPr-cas gene editing. *Nat. Mater.* **20**, 701-+ (2021).

27. K. J. Kauffman, M. a. oberli, J. r. dorkin, J. e. hurtado, J. c. Kaczmarek, S. Bhadani, J. Wyckoff, r. langer, a. Jaklenec, d. G. anderson, rapid, single-cell analysis and discovery of vectored mrna transfection in vivo with a loxP-flanked tdTomato reporter mouse. *Mol. Ther.-Nucl. Acids.* **10**, 55–63 (2018).

28. J. c. Kaczmarek, K. J. Kauffman, o. S. Fenton, K. Sadder, a. K. Patel, M. W. heartlein, F. derosa, d. G. anderson, optimization of a degradable polymer-lipid nanoparticle for potent systemic delivery of mrna to the lung endothelium and immune cells. *Nano Lett.* **18**, 6449–6454 (2018).

29. M. Qiu, Y. Tang, J. chen, r. Muriph, Z. Ye, c. huang, J. evans, e. P. henske, Q. Xu, lung-selective mrna delivery of synthetic lipid nanoparticles for the treatment of pulmonary lymphangioleiomyomatosis. *Proc. Natl. Acad. Sci. U.S.A.* **119**, e2116271119 (2022).

30. J. c. Melms, J. Biermann, h. huang, Y. Wang, a. nair, S. Tagore, i. Katsyv, a. F. rendeiro, a. d. amin, d. Schapiro, c. J. Frangieh, a. M. luoma, a. Filliol, Y. Fang, h. ravichandran, M. G. clausi, G. a. alba, M. rogava, S. W. chen, P. ho, d. T. Montoro, a. e. Kornberg, a. S. han, M. F. Bakhoum, n. anandasabapathy, M. Suarez-Farinas, S. F. Bakhoum, Y. Bram, a. Borczuk, X. V. Guo, J. h. lefkowitch, c. Marboe, S. M. lagana, a. del Portillo, e. J. Tsai, e. Zorn, G. S. Markowitz, r. F. Schwabe, r. e. Schwartz, o. elemento, a. Saqi, h. hibshoosh, J. Que, B. izar, a molecular single-cell lung atlas of lethal coVid-19. *Nature* **595**, 114–119 (2021).

31. P. levéen, J. larsson, M. ehinger, c. M. cilio, M. Sundler, l. J. Sjöstrand, r. holmdahl, S. Karlsson, induced disruption of the transforming growth factor beta type ii receptor gene in mice causes a lethal inflamm tory disorder that is transplantable. *Blood* **100**, 560–568 (2002).

32. d. c. liberti, M. M. Kremp, W. a. liberti, i. J. Penkala, S. r. li, S. Zhou, e. e. Morrisey, alveolar epithelial cell fate is maintained in a spatially restricted manner to promote lung regeneration after acute injury. *Cell Rep.* **35**, 109092 (2021).

33. l. V. ellis, M. P. cain, V. hutchison, P. Flodby, e. d. crandall, Z. Borok, B. Zhou, e. J. ostrin, J. d. Wythe, J. c. chen, epithelial Vegfa specifies a distin t endothelial population in the mouse lung. *Dev. Cell* **52**, 617–630.e6 (2020).

34. a. Gillich, F. Zhang, c. G. Farmer, K. J. Travaglini, S. Y. Tan, M. Gu, B. Zhou, J. a. Feinstein, M. a. Krasnow, r. J. Metzger, capillary cell-type specialization in the alveolus. *Nature* **586**, 785–789 (2020).

35. n. S. Mangalmurti, J. l. Friedman, l.-c. Wang, d. Stolz, G. Muthukumaran, d. l. Siegel, a. M. Schmidt, J. S. lee, S. M. albelda, The receptor for advanced glycation end products mediates lung endothelial activation by rBcs. *Am. J. Physiol.-Lung Cell. Mol. Physiol.* **304**, l250–l263 (2013).

36. X. Wang, S. abraham, J. a. McKenzie, n. Jeffs, M. Swire, V. B. Tripathi, U. F. luhmann, c. a. lange, Z. Zhai, h. M. arthur, J. Bainbridge, S. e. Moss, J. Greenwood, lrG1 promotes angiogenesis by modulating endothelial TGF-β signalling. *Nature* **499**, 306–311 (2013).

37. r. Fu, Y. li, n. Jiang, B. X. ren, c. Z. Zang, l. J. liu, W. c. lv, h. M. li, S. Weiss, Z. Y. li, T. lu, Z. Q. Wu, inactivation of endothelial ZeB1 impedes tumor progression and sensitizes tumors to conventional therapies. *J. Clin. Invest.* **130**, 1252–1270 (2020).

38. r. a. Wimmer, a. leopoldi, M. aichinger, d. Kerjaschki, J. M. Penninger, Generation of blood vessel organoids from human pluripotent stem cells. *Nat. Protoc.* **14**, 3082–3100 (2019).

39. e. Willems, J. cabral-Teixeira, d. Schade, W. cai, P. reeves, P. J. Bushway, M. lanier, c. Walsh, T. Kirchhausen, J. c. izpisua Belmonte, J. cashman, M. Mercola, Small molecule-mediated TGF-β type ii receptor degradation promotes cardiomyogenesis in embryonic stem cells. *Cell Stem Cell* **11**, 242–252 (2012).

40. K. a. hajj, r. l. Ball, S. B. deluty, S. r. Singh, d. Strelkova, c. M. Knapp, K. a. Whitehead, Branched-tail lipid nanoparticles potently deliver mrna in vivo due to enhanced ionization at endosomal ph. *Small* **15**, e1805097 (2019).

41. r. S. riley, M. V. Kashyap, M. M. Billingsley, B. White, M.-G. alameh, S. K. Bose, P. W. Zoltick, h. li, r. Zhang, a. Y. cheng, d. Weissman, W. h. Peranteau, M. J. Mitchell, ionizable lipid nanoparticles for in utero mrna delivery. *Sci. Adv.* **7**, eaba1028 (2021).

42. M. Jayaraman, S. M. ansell, B. l. Mui, Y. K. Tam, J. chen, X. du, d. Butler, l. eltepu, S. Matsuda, J. K. narayanannair, K. G. rajeev, i. M. hafez, a. akinc, M. a. Maier, M. a. Tracy, P. r. cullis, T. d. Madden, M. Manoharan, M. J. hope, Maximizing the potency of sirna lipid nanoparticles for hepatic gene silencing in vivo. *Angew. Chem. Int. Ed. Engl.* **51**, 8529–8533 (2012).

43. l. Madisen, T. a. Zwingman, S. M. Sunkin, S. W. oh, h. a. Zariwala, h. Gu, l. l. ng, r. d. Palmiter, M. J. hawrylycz, a. r. Jones, e. S. lein, h. Zeng, a robust and high-throughput cre reporting and characterization system for the whole mouse brain. *Nat. Neurosci.* **13**, 133–140 (2010).

44. d. Bates, S. harper, regulation of vascular permeability by vascular endothelial growth factors. *Vascul. Pharmacol.* **39**, 225–237 (2002).

45. i. Kosmidou, d. Karmpaliotis, a. J. Kirtane, h. V. Barron, c. M. Gibson, Vascular endothelial growth factors in pulmonary edema: an update. *J. Thromb. Thrombolysis* **25**, 259–264 (2008).

46. h. Parhiz, J. S. Brenner, P. n. Patel, T. e. Papp, h. Shahnawaz, Q. li, r. Shi, M. e. Zamora, a. Yadegari, o. a. Marcos-contreras, added to pre-existing inflammtion, mrna-lipid nanoparticles induce inflammtion exacerbation (ie). *J. Control. Release* **344**, 50–61 (2022).

47. S. dimmeler, a. M. Zeiher, endothelial cell apoptosis in angiogenesis and vessel regression. *Circ. Res.* **87**, 434–439 (2000).

48. i. Friehs, r. Barillas, n. V. Vasilyev, n. roy, F. X. McGowan, P. J. del nido, Vascular endothelial growth factor prevents apoptosis and preserves contractile function in hypertrophied infant heart. *Circulation* **114**, i290–i295 (2006).

49. c. hanumegowda, l. Farkas, M. Kolb, angiogenesis in pulmonary fibrosis. *Chest* **142**, 200–207 (2012).

50. Q. hong, l. Zhang, J. Fu, d. a. Verghese, K. chauhan, G. n. nadkarni, Z. li, W. Ju, M. Kretzler, G.-Y. cai, X.-M. chen, V. d. d'agati, S. G. coca, d. Schlondorff, J. c. he, K. lee, lrG1 promotes diabetic kidney disease progression by enhancing TGF-β–induced angiogenesis. *J. Am. Soc. Nephrol.* **30**, 546–562 (2019).

51. c. camilli, a. e. hoeh, G. de rossi, S. e. Moss, J. Greenwood, lrG1: an emerging player in disease pathogenesis. *J. Biomed. Sci.* **29**, 6 (2022).

52. J. a. nagy, a. M. dvorak, h. F. dvorak, VeGF-a and the induction of pathological angiogenesis. *Annu. Rev. Pathol. Mech. Dis.* **2**, 251–275 (2007).

53. X. huang, X. Zhang, n. Machireddy, c. e. evans, S. d. Trewartha, G. hu, Y. Fang, G. M. Mutlu, d. Wu, Y. Y. Zhao, endothelial FoxM1 reactivates aging-impaired endothelial regeneration for vascular repair and resolution of inflammtory lung injury. *Sci. Transl. Med.* **15**, eabm5755 (2023).

54. i. Sörensen, r. h. adams, a. Gossler, dll1-mediated notch activation regulates endothelial identity in mouse fetal arteries. *Blood* **113**, 5680–5688 (2009).

55. a. i. Weiner, S. r. Jackson, G. Zhao, K. K. Quansah, J. n. Farshchian, K. M. neupauer, e. Q. littauer, a. J. Paris, d. c. liberti, G. S. Worthen, e. e. Morrisey, a. e. Vaughan, Mesenchyme-free expansion and transplantation of adult alveolar progenitor cells: Steps toward cell-based regenerative therapies. *NPJ Regen. Med.* **4**, 17 (2019).

56. e. Zudaire, l. Gambardella, c. Kurcz, S. Vermeren, a computational tool for quantitative analysis of vascular networks. *PLOS ONE* **6**, e27385 (2011).

57. J. Kalucka, l. P. M. h. de rooij, J. Goveia, K. rohlenova, S. J. dumas, e. Meta, n. V. conchinha, F. Taverna, l. a. Teuwen, K. Veys, M. Garcia-caballero, S. Khan, V. Geldhof, l. Sokol, r. Y. chen, l. Treps, M. Borri, P. de Zeeuw, c. dubois, T. K. Karakach, K. d. Falkenberg, M. Parys, X. K. Yin, S. Vinckier, Y. X. du, r. a. Fenton, l. Schoonjans, M. dewerchin, G. eelen, B. Thienpont, l. lin, l. Bolund, X. r. li, Y. l. luo, P. carmeliet, Single-cell transcriptome atlas of murine endothelial cells. *Cell* **180**, 764–779.e20 (2020).

*Zhao et al., Sci. Transl. Med.* **16**, eadg6229 (2024) 31 January 2024

**15 of 15**